bioRxiv preprint doi: https://doi.org/10.1101/2020.10.01.321604; this version posted October 1, 2020. The copyright holder for this preprint (which was not certified by peer review) is the author/funder, who has granted bioRxiv a license to display the preprint in perpetuity. It is made available under aCC-BY-NC-ND 4.0 International license.

# Selection for increased tibia length in mice alters skull shape through parallel changes in developmental mechanisms

Colton M. Unger[1,3], Jay Devine[4], Benedikt Hallgrímsson [3,4,5], and Campbell Rolian[2,3*]

[1] Department of Biological Sciences, University of Calgary, Calgary, AB T2N 4N1, Canada.

[2] Department of Comparative Biology and Experimental Medicine, Faculty of Veterinary Medicine, University of Calgary, AB T2N4N1, Canada.

[3] McCaig Institute for Bone and Joint Health, Calgary, AB T2N4N1, Canada.

[4] Department of Cell Biology and Anatomy, University of Calgary, Calgary, AB, Canada.

[5]Alberta Children's Hospital Research Institute for Child and Maternal Health, University of Calgary, Calgary, AB, Canada.

*Corresponding author: Tel.: +1 (403) 210-3888 or Email: cprolian@ucalgary.ca

bioRxiv preprint doi: https://doi.org/10.1101/2020.10.01.321604; this version posted October 1, 2020. The copyright holder for this preprint (which was not certified by peer review) is the author/funder, who has granted bioRxiv a license to display the preprint in perpetuity. It is made available under aCC-BY-NC-ND 4.0 International license.

**Abstract**

Many bones in the vertebrate skeleton, including the limb bones, axial skeleton, and bones of the floor of the cranium, grow through the process of endochondral ossification, under the control of growth plates. The cellular and molecular mechanisms of endochondral ossification are conserved across these cartilaginous growth plates, increasing the tendency of skeletal elements to covary in size and shape. Covariation at the phenotypic, developmental, and genetic levels has been hypothesized to lead to correlated changes in parts of the skeleton not under direct selection. We tested this hypothesis using the selectively bred Longshanks mouse, in which the sole target of selection was relative tibia length. We use x-ray micro-computed tomography (μCT) and geometric morphometrics in a large, multi-generation sample of Longshanks and random-bred wildtype mice to characterize shape changes in the Longshanks cranium. We show that Longshanks skulls became longer, flatter, and narrower in a stepwise intergenerational process. Moreover, we show that these morphological changes likely resulted from underlying developmental changes in the growth plates of the cranial base, that mirror changes in the process of endochondral ossification observed in Longshanks' tibia growth plate. Taken together, these results show that indirect, and potentially non-adaptive, skeletal changes can occur due to developmental overlap among distant anatomical elements, with important implications for interpreting the evolutionary history of vertebrate skeletal form.

bioRxiv preprint doi: https://doi.org/10.1101/2020.10.01.321604; this version posted October 1, 2020. The copyright holder for this preprint (which was not certified by peer review) is the author/funder, who has granted bioRxiv a license to display the preprint in perpetuity. It is made available under aCC-BY-NC-ND 4.0 International license.

## Introduction

Organismal development is a major determinant of phenotypic variation, and therefore is fundamentally related to how organisms evolve (Hendrikse, Parsons and Hallgrímsson, 2007; Hallgrímsson and Lieberman, 2008). Organisms are comprised of interrelated anatomical elements whose morphology is patterned by shared genetic pathways (i.e., pleiotropic genes) and often by the same developmental processes (Hallgrímsson and Hall, 2005; Murren, 2012). Shared genetic and/or developmental processes lead to morphological integration, that is, the tendency of sets of traits to covary more strongly internally than with traits in other sets (Cheverud, 1996). In turn, integrated individual anatomical structures contribute to the modular organization of biological systems (Wagner, Pavlicev and Cheverud, 2007; Hallgrímsson *et al.*, 2009).

If two anatomical structures are integrated due to underlying genetic phenomena, such as pleiotropy or linkage disequilibrium, then those traits are more likely to respond to selection in a concerted manner (Armbruster and Schwaegerle, 1996; Cheverud, 1996). As a result of integration, correlated responses to selection can result in phenotypic changes in some traits that are merely a consequence of covariation with other traits under selection (Gould and Lewontin, 1979; Wagner, 1984; Price and Langen, 1992; Parsons *et al.*, 2015). Understanding how developmental processes lead to correlated responses to selection is pivotal to distinguishing adaptive changes from those that are non-adaptive, or potentially even maladaptive, in analyses of phylogeny, ancestral relationships and evolutionary change within lineages (Gould and Lewontin, 1979; Riska, 1986; von Cramon-Taubadel, 2019).

The bones of the terrestrial vertebrate cranial floor (basicranium) and the postcranial skeleton represent an interesting case of integration because they are physically distant, yet both develop

bioRxiv preprint doi: https://doi.org/10.1101/2020.10.01.321604; this version posted October 1, 2020. The copyright holder for this preprint (which was not certified by peer review) is the author/funder, who has granted bioRxiv a license to display the preprint in perpetuity. It is made available under aCC-BY-NC-ND 4.0 International license.

by the process of endochondral ossification (EO) (De Beer, 1937; White and Wallis, 2001; Mackie *et al.*, 2008). There is therefore the potential for evolutionary changes in one structure to cause correlated phenotypic changes in the other. EO proceeds through the formation, expansion, and mineralization of a cartilaginous template, known as an anlage, that is patterned *in utero* and undergoes post-natal longitudinal expansion (Kronenberg, 2003; Mackie *et al.*, 2008; Lefebvre and Bhattaram, 2010; Roselló-Díez and Joyner, 2015). In the limbs, ossification initiates by the formation of primary and secondary ossification centers and continues into post-natal development via specialized growth plates situated at the ends of the long bones (Kronenberg, 2003; Mackie *et al.*, 2008; Lefebvre and Bhattaram, 2010). The postcranial growth plate, once formed, is comprised of three histologically distinct zones containing cartilage-producing cells (chondrocytes) in different physiological states: resting, proliferative, and hypertrophic (Roselló-Díez and Joyner, 2015).

The basicranium is comprised of three bones: the basioccipital, the basisphenoid, and the presphenoid, which make up the floor of the caudal portion of the skull in mammals and are formed by growth in the spheno-occipital (SOS) and intersphenoidal (ISS) synchondroses (Wei *et al.*, 2016). Synchondroses are structurally analogous to growth plates, however, synchondroses grow bidirectionally and have duplicated proliferative and hypertrophic zones (Wei *et al.*, 2016). Basicranial growth is thought to be a key determinant of overall skull shape. The basicranium is the first cranial skeletal element to develop and is controlled intrinsically by EO-like mechanisms, whereas the face and calvarium are influenced by, and grow in response to, hormonal regulation of surrounding tissue and brain growth, respectively (Scott, 1958; Waters and Kaye, 2002; Bastir and Rosas, 2006; Richtsmeier *et al.*, 2006). Additionally, the basicranium

bioRxiv preprint doi: https://doi.org/10.1101/2020.10.01.321604; this version posted October 1, 2020. The copyright holder for this preprint (which was not certified by peer review) is the author/funder, who has granted bioRxiv a license to display the preprint in perpetuity. It is made available under aCC-BY-NC-ND 4.0 International license.

supports the brain and contains critical foramina for the passage of vasculature and cranial nerves and is therefore central to proper craniofacial development (Lieberman *et al.*, 2008).

Here, we used the Longshanks mouse to study correlated evolution of cranial and post-cranial skeletal elements. The Longshanks mouse was established through artificial selection for increased tibia length relative to body mass, using an outbred CD1 stock. By generation 20, mean tibia length in two independently selected Longshanks lines had increased by 13-15% in comparison to random-bred Controls from the same genetic background with no change in average body mass (Marchini *et al.*, 2014; Castro *et al.*, 2019). Investigation of the cellular mechanisms governing limb development in Longshanks revealed structural alterations in the postnatal epiphyseal growth plate of the tibia. Specifically, the Longshanks selection regime resulted in larger tibial growth plates with larger resting and proliferative zones, without changes in cell division rate or timing of growth plate fusion compared to Controls (Marchini and Rolian, 2018). Previous analyses also suggested the tibia selection regime resulted in mice that are skeletally larger in relation to body mass, with correlated skeletal responses at the systemic level (Sparrow *et al.*, 2017), along with potentially maladaptive changes in skeletal microarchitecture (Farooq *et al.*, 2017; Cosman, Britz and Rolian, 2019).

The Longshanks experiment offers a unique opportunity to study correlated evolution in skeletal traits that were not directly under selection, in a model with known evolutionary history, under controlled laboratory settings. Given the underlying developmental relationship between the long bones and cranial base, we investigated whether selection for increased tibia length indirectly altered the shape of the Longshanks cranium. We tested the general hypothesis that selection for increased tibia length produced indirect responses in the cranium of Longshanks through changes to the shared process of endochondral ossification. Specifically, we predicted that Longshanks

bioRxiv preprint doi: https://doi.org/10.1101/2020.10.01.321604; this version posted October 1, 2020. The copyright holder for this preprint (which was not certified by peer review) is the author/funder, who has granted bioRxiv a license to display the preprint in perpetuity. It is made available under aCC-BY-NC-ND 4.0 International license.

crania will have a series of craniofacial morphological changes corresponding to altered synchondrosis size/architecture. To test this hypothesis, we compared the 3D shape of adult Longshanks crania from both Longshanks lines to Controls across three evenly spaced generations in the selection experiment. We also used a combination of morphometric analysis and histology to investigate cranial development in Longshanks neonates.

## Materials and Methods

### Animal samples

All animal procedures were approved by the Health Sciences Animal Care Committee at the University of Calgary (AC13-0077) and (AC17-0026) and performed in accordance with best practices outlined by the Canadian Council on Animal Care. For more information on the husbandry methods and selective Longshanks breeding regimen, see Marchini *et al*. (2014).

We collected 8-week old, non-breeder Longshanks mice (N=327) from generations 1, 9, and 20 across three experimental lines: Longshanks 1 (hereafter LS1), Longshanks 2 (LS2), and Control (CTL) to study changes in adult cranial shape at the beginning, middle, and end of the selection process, respectively (Table 1). Each group was as sex and family balanced as possible to account for differences due to sexual dimorphism and/or family diversity (Karp *et al.*, 2017). To investigate the developmental basis of the Longshanks cranium, we generated postnatal day seven (P07) neonates (N=104) from F31 Longshanks mice (Table 1). The three lines have not actively undergone artificial selection since generation F22 and are maintained as experimental populations. We selected P07 as our developmental time point as this is when Longshanks tibiae

bioRxiv preprint doi: https://doi.org/10.1101/2020.10.01.321604; this version posted October 1, 2020. The copyright holder for this preprint (which was not certified by peer review) is the author/funder, who has granted bioRxiv a license to display the preprint in perpetuity. It is made available under aCC-BY-NC-ND 4.0 International license.

are growing fastest, and the cranial skeleton is still actively growing (Vora, Camci and Cox, 2016; Farooq *et al.*, 2017; Marchini and Rolian, 2018).

**X-ray Micro-Computed Tomography (µCT)**

We performed X-ray micro-computed tomography (µCT). We used a Skyscan 1173 v1.6 µCT scanner (Bruker, Kontich, Belgium) to acquire whole-body scans of the adults and separate scans of the neonate cranium and tibiae. We obtained adult samples from frozen archived carcasses at each generation, while F32 neonates were scanned the day they were euthanized. In addition, we scanned the corresponding right hindlimb of each neonate that underwent cranium scanning. Adult scans were acquired at 70-80 kV and 60-75 µA with 44.73 µm isotropic voxels and no filter, while neonates were scanned at a resolution of 17.04 µm isotropic voxels with otherwise identical parameters. Stack reconstructions were performed using NRecon v1.7.4.2 (Bruker, Kontich, Belgium).

**Histology**

We dissected neonate crania after scanning them and fixed them in 10% neutral buffered formalin (NBF) (Thermo Scientific) for 48 hours, with NBF replacement every 24 hours. Fixed cranium tissues were then transferred to a decalcifying solution (Cal-Ex II™, Fisher Chemical) for 72 hours with daily solution changes. After decalcification, a rectangular portion of the cranial base containing both basicranial synchondroses was dehydrated, embedded it in paraffin, and sectioned in the sagittal plane at 12 µm. Sections were deparaffinized in Slide Brite™ (Jones Scientific Products, Inc.) and subsequently stained. The slides of a specimen were stained in an alternating fashion with two stains: (1) Wiegert's Iron Haematoxylin (Sigma), 0.05% Fast-Green (FCF) (Sigma), counterstained in 0.1% Safranin-o solution (Sigma); or (2) Gill's Haematoxylin

bioRxiv preprint doi: https://doi.org/10.1101/2020.10.01.321604; this version posted October 1, 2020. The copyright holder for this preprint (which was not certified by peer review) is the author/funder, who has granted bioRxiv a license to display the preprint in perpetuity. It is made available under aCC-BY-NC-ND 4.0 International license.

#3 (Sigma), rinsed in 70% ethanol, and counterstained with 1% alcoholic Eosin Y (Sigma). We imaged sagittal midline sections using an Axio Scan.Z1 slide scanner (Ziess, Oberkochen, Germany) at 10x magnification and qualitatively evaluated differences in growth plate size and morphology.

**Landmarking**

μCT adult and neonate crania scans were subjected to a novel image registration-based pipeline to automatically detect landmarks for a geometric morphometrics (GM) shape analysis (Percival *et al.*, 2019). Automated landmarking improves data standardization and can be used to quickly process very large sample sizes while reducing intraobserver errors, such as landmark placement drift (Fruciano, 2016; Devine *et al.*, 2020). Automated landmarking involves volumetric registration using a global affine alignment of the skull volumes, followed by a dense non-linear deformation between each cranium and a reference atlas. Here, the atlas is an average volume, with a standardized landmark configuration, that best minimizes intensity differences from the rest of the sample. We used 68 3D landmarks for the adults and 50 3D landmarks for the neonates (Supplementary Figure S1 and S2; Supplementary Tables S1 and S2).

We computed the affine transformations with a multi-resolution framework, where the μCT volumes are translated, scaled, rotated, and sheared at progressively higher resolutions until their affine alignment with the atlas is maximized (Lerch, Sled and Henkelman, 2010). We computed the non-linear transformations with the multi-resolution SyN (Symmetric Normalization) algorithm (Avants *et al.*, 2011), which involves symmetrically flowing an image pair into one another along a velocity field. We then recovered, concatenated, and inverted the transformations, and finally propagated the atlas landmarks along this path to the original image

bioRxiv preprint doi: https://doi.org/10.1101/2020.10.01.321604; this version posted October 1, 2020. The copyright holder for this preprint (which was not certified by peer review) is the author/funder, who has granted bioRxiv a license to display the preprint in perpetuity. It is made available under aCC-BY-NC-ND 4.0 International license.

space for analysis. All image processing was performed with the open-source MINC (Medical Imaging NetCDF) toolkit (https://github.com/BIC-MNI/minc-toolkit-v2).

In addition to investigating overall neonate cranium shape, we characterized cranial base shape with two-dimensional (2D) landmarks at the sagittal midline. We used a 12 landmark set highlighting the vertices of the developing basicranial bones which provides information about the shape of the sagittal cross-section of the basicranial synchondroses (Supplemental Figure S3; Supplementary Table S3). Landmarks at the midline were placed in Amira v.5.4.2 (Visage Imaging, Berlin, Germany) by one observer (CMU) blind to the identity of the specimens. Adult tibiae lengths were quantified in Amira by calculating the distance, in mm, between two landmarks that we placed on the distal tip of the lateral malleolus and most lateral point on the proximal epiphysis, two anatomical points that were demonstrated to have high homology and repeatability (Cosman, Sparrow and Rolian, 2016). Because neonate tibia length is not fully visible in the scans due to small or absent secondary ossification centers (Moss, 1977), neonate tibia measurements were obtained from the distance, in mm, between landmarks placed on the distal and proximal ends of the ossified tibial diaphysis on the rostral edge along the sagittal midline of the tibia.

**Geometric Morphometrics**

Analyses were performed on the R/Rstudio computational platform (R Core Team, 2020). We investigated shape cranial differences by superimposing the adult and neonate landmark configurations into age-specific morphospaces via Generalized Procrustes Analysis (GPA). To study the influence of selection on cranial shape, we first corrected for confounding variables known to alter adult and neonatal morphology.

bioRxiv preprint doi: https://doi.org/10.1101/2020.10.01.321604; this version posted October 1, 2020. The copyright holder for this preprint (which was not certified by peer review) is the author/funder, who has granted bioRxiv a license to display the preprint in perpetuity. It is made available under aCC-BY-NC-ND 4.0 International license.

In the adult dataset, we controlled for the effects of sex and size. Upon regressing shape on sex, we observed that sex accounted for a small but significant amount of variation (2.2%), although there were no sex-specific differences in cranial responses to selection (data not shown). Using sex-adjusted residuals, we investigated allometry in the Longshanks cranium to parse out how much of the cranial selection response, if any, could be attributed to changes in skeletal size. While Procrustes superimposition removes scale, it does not account for differences in biological shape that are associated with size i.e. allometry (Klingenberg, 2016). Because Longshanks mice are skeletally larger in relation to body mass in the post-cranium (Sparrow *et al.*, 2017), we employed a pooled within-group analysis of covariance (ANCOVA) of cranium centroid size on body mass to determine whether the same trend exists in the Longshanks cranium. Mean centroid size after accounting for body mass was significantly different among lines at F20 ($F = 22.83$, $p < 0.001$), with Longshanks LS1 and LS2 lines having larger crania than Controls (Supplementary Figure S4) (Tukey's post-hoc test, LS1vsLS2 $p = 0.460$, LS1vsCTL $p < 0.001$, LS2vsCTL $p < 0.001$). There was no difference in mean centroid size, after controlling for covariation with body mass, among founder (F01) samples (Supplementary Figure S4) ($F = 0.1998$, $p = 0.819$).

For the neonate dataset, we controlled for the effects of litter size but not sex, due to uncertainties in assigning sex anatomically in neonates. After regressing cranial size and tibia length on litter size, we observed a strong negative correlation ($r = -0.72$, $p < 0.001$). LS2, which had litter sizes that were ~2 pups larger than LS1 and ~4 pups larger than controls on average, exhibited significantly smaller centroid sizes than LS1 and Controls (Tukey's post-hoc test, LS1vsLS2 $p < 0.001$, LS1vsCTL $= 0.764$, LS2vsCTL $p < 0.001$) (Supplementary Figure S5;

bioRxiv preprint doi: https://doi.org/10.1101/2020.10.01.321604; this version posted October 1, 2020. The copyright holder for this preprint (which was not certified by peer review) is the author/funder, who has granted bioRxiv a license to display the preprint in perpetuity. It is made available under aCC-BY-NC-ND 4.0 International license.

Supplementary Table S4). Thus, we performed our neonate analyses with Procrustes shape variables and univariate measurements, such as tibia length, adjusted for litter size effects.

Group differences in adult and neonate cranial morphology were evaluated using principal component analyses (PCA). We assessed whether group mean shapes, independent of size and/or sex, were statistically significantly different using a randomized residual (1000 permutations) Procrustes ANCOVA (Goodall, 1991; Collyer, Sekora and Adams, 2015). Post-hoc pairwise tests compared differences in least-squares means between groups (Collyer and Adams, 2018). For visualizations of cranial shape differences between lines, we used deformation heatmaps and cranial meshes with vectors of shape change that depict transformations between group means. All GM analyses were performed in R with the *geomorph*, *Morpho,* and *RRPP* packages (Schlager, 2017, 2020; Collyer and Adams, 2018; Adams, Collyer and Kaliontzopoulou, 2020).

bioRxiv preprint doi: https://doi.org/10.1101/2020.10.01.321604; this version posted October 1, 2020. The copyright holder for this preprint (which was not certified by peer review) is the author/funder, who has granted bioRxiv a license to display the preprint in perpetuity. It is made available under aCC-BY-NC-ND 4.0 International license.

## Results

### Longshanks Adults

*Body mass and cranium size allometry is altered in Longshanks adults*

F01 mice (founders) that had not been subjected to selection did not differ in average weight or tibia length between lines (Supplementary Figure S6; Supplementary Table S5). Moreover, random-bred F09 Controls and F20 Controls did not differ from F01 founders in terms of tibia length (Supplementary Figure S6; Supplementary Table S5). In contrast, LS1 and LS2 at F09 have an average of 7.3% longer tibiae compared to F09 Controls, while LS1 and LS2 at F20 have 16.4% longer tibiae on average when compared to F20 Controls (Supplementary Figure S6; Supplementary Table S5). Average body mass in our sample was stable between lines across all three generations and did not differ significantly in all but two pairwise comparisons between groups (Supplementary Figure S6; Supplementary Table S5). In contrast, at generation F20, LS1 and LS2 mice had significantly larger cranium centroid sizes than Controls (Tukey's post-hoc test, F20 LS1vsF20 CTL $p < 0.05$, F20 LS2vsF20 CTL $p < 0.05$), though the latter did not differ from F01 or F09 Controls (Tukey's post-hoc test, F01 CTLvsF09 CTL $p = 0.566$, F09 CTLvsF20 CTL $p = 0.276$, F01 CTLvsF20 CTL $p = 0.999$).

Given that the long bones of the Longshanks post-cranial skeleton are larger than Controls at any given body mass (Sparrow *et al*. 2017), we asked if the allometric scaling relationship between Longshanks crania and overall body mass had changed in response to 20 generations of selection. ANCOVA comparing mean cranium centroid size among lines using body mass as the covariate indicates that body mass is significantly correlated with cranium centroid size ($r = 0.697$, $p < 0.001$). There was a significant difference in centroid size between Controls and

bioRxiv preprint doi: https://doi.org/10.1101/2020.10.01.321604; this version posted October 1, 2020. The copyright holder for this preprint (which was not certified by peer review) is the author/funder, who has granted bioRxiv a license to display the preprint in perpetuity. It is made available under aCC-BY-NC-ND 4.0 International license.

Longshanks after controlling for covariation with body mass, however LS1 and LS2 did not differ from each other (Tukey's post-hoc test, LS1vsLS2 $p = 0.460$, LS1vsCTL $p < 0.001$, LS2-CTL $p < 0.001$). Hence, Longshanks selected lines have skeletally larger crania after 20 generations of selection independent of body mass (Supplementary Figure S4).

*The Longshanks cranium is longer, narrower, and flatter*

Next, we asked if the fact that tibia length and cranium centroid size increases in F20 LS1 and LS2 is associated with shape differences in their cranium compared to F09 and F01 mice. We performed a principal component analysis (PCA) on the residuals of a multivariate regression of shape on sex in order to control for potential sex effects on cranial shape in our sample. Comparison of PC score means between groups demonstrates that despite overlap in skull shape, LS1 and LS2 have shifted substantially into positive PC1 space, reflecting crania that are longer and narrower with reduction in vault height (Figure 1A). Post-hoc pairwise comparisons from a Procrustes ANCOVA comparing adult cranium shape by group, independent of sex effects, showed that all groups within line by generation, or within generation by line, differ in mean shape, except F01 LS2 and Controls (F01 LS2 vs F01 CTL $p = 0.203$). When comparing the Euclidean distance among group sex-adjusted PC score means, however, F20 LS1 and LS2 mice are on average over twice as far from unselected mice in morphospace (i.e., all F01 founders, F09 and F20 controls) than the latter are from each other (mean Euclidean distances 0.023 vs 0.010, Supplementary Table S6)

bioRxiv preprint doi: https://doi.org/10.1101/2020.10.01.321604; this version posted October 1, 2020. The copyright holder for this preprint (which was not certified by peer review) is the author/funder, who has granted bioRxiv a license to display the preprint in perpetuity. It is made available under aCC-BY-NC-ND 4.0 International license.

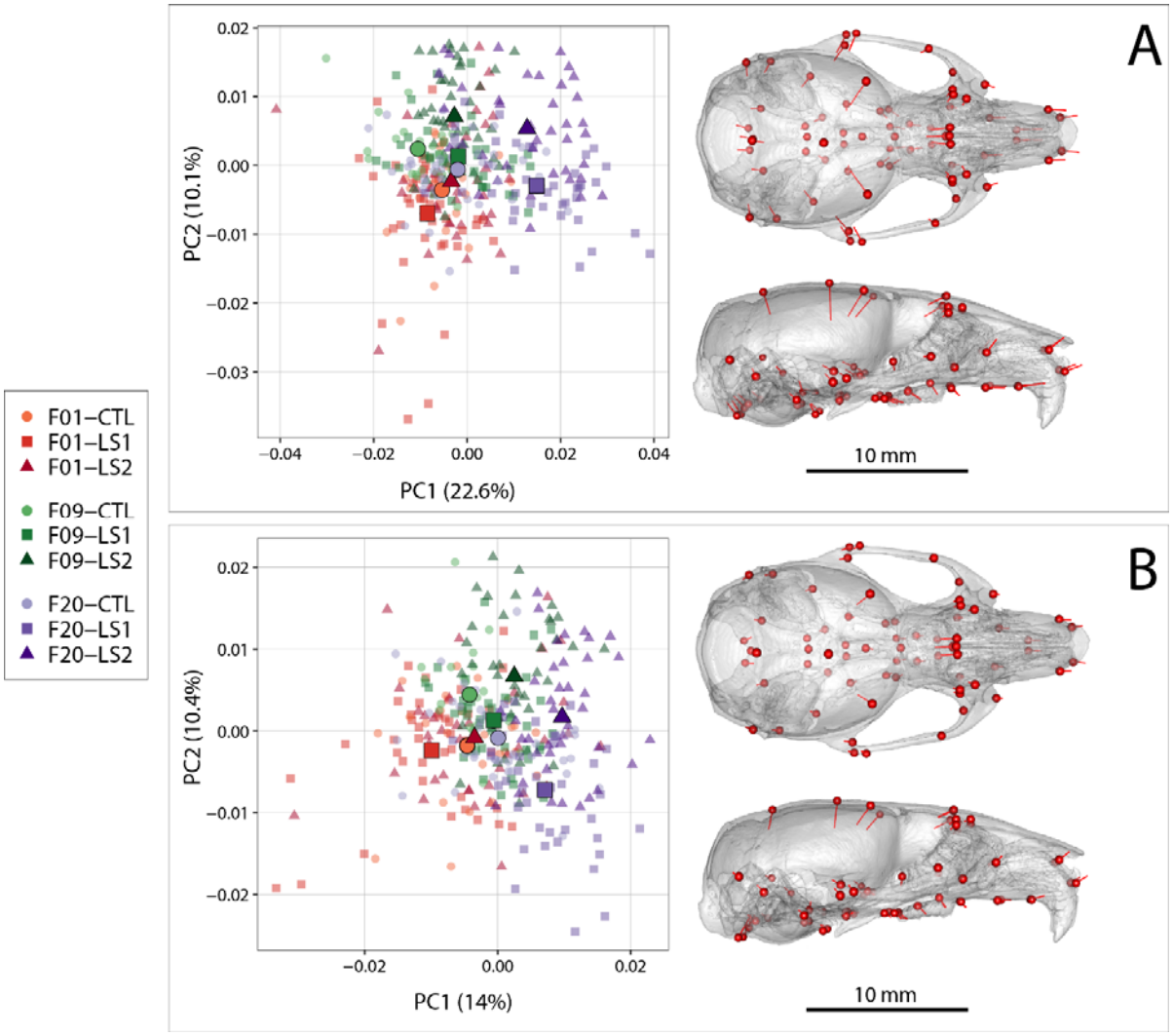


**Figure 1** – Scatter plots of the first two principal components (PC) of Procrustes shape variables in adult Longshanks and Controls throughout the selection process. (A) Plot of sex-adjusted Procrustes shape variables (left), and vectors of shape change at each cranium landmark (magnified 2 times for visualization) showing shape transformations along PC1 from negative to positive scores (right). Large symbols indicate mean PC1 and PC2 scores for each respective cohort. (B) Plot of Procrustes shape variables additionally corrected for size.

bioRxiv preprint doi: https://doi.org/10.1101/2020.10.01.321604; this version posted October 1, 2020. The copyright holder for this preprint (which was not certified by peer review) is the author/funder, who has granted bioRxiv a license to display the preprint in perpetuity. It is made available under aCC-BY-NC-ND 4.0 International license.

*Longshanks cranial shape differences remain after controlling for skull size and sex*

Given that PC1 generally captures differences in shape primarily due to allometric effects of size (Klingenberg, 2016), and that LS1 and LS2 have larger skulls in F20, we asked if the cranium of F20 selected lines score more positively simply because they are larger, and if larger skulls are associated with different cranium shapes in F20 selected lines compared to Controls and F01 unselected lines. We compared the fitted PC1 scores of a pooled-within group regression of shape on size to log (centroid size), which shows the cranium size and shape scaling relationship, between all nine groups in our sample (Supplementary Figure S7). At any given centroid size, Longshanks F20 selected lines score more positively (longer and narrower) in predicted shape. Importantly, the slopes of the lines, which capture the scaling relationship between cranium shape and size did not differ significantly between any of the groups in our sample ($p > 0.05$). Thus, while Longshanks F20 LS1 and LS2 have larger crania at any given body mass compared to Controls, the allometric pattern within the cranium itself was not altered by selection for increased tibia length.

The difference in intercept between the fitted PC1 scores and log centroid size of LS1 and LS2 in relation to Controls (Supplementary Figure S7) suggest that while the increase in size of F20 selected crania contributes to the shape differences along PC1, it is not the only cause of shape variation. We therefore asked if differences in shape between the Longshanks and Control cohorts persist when the effect of size is removed from our sample by using multivariate regression residuals of shape on size. The PCA of shape independent of size and sex shows a marked reduction in group separation along PC1; however, F20 LS1 and LS2 still typically score more positively in PC1, corresponding to crania that are relatively longer, narrower, and have reduction in vault height (Figure 1B). Post-hoc pairwise comparisons from a Procrustes

bioRxiv preprint doi: https://doi.org/10.1101/2020.10.01.321604; this version posted October 1, 2020. The copyright holder for this preprint (which was not certified by peer review) is the author/funder, who has granted bioRxiv a license to display the preprint in perpetuity. It is made available under aCC-BY-NC-ND 4.0 International license.

ANCOVA comparing adult cranium shape by group independent of size and sex effects showed that all groups within line by generation, or within generation by line, differ in mean shape ($F = 8.205$, $p < 0.001$) except F01 LS2 and Controls (F01 LS2 – F01 CTL $p = 0.173$). As with sex-adjusted data, F20 Longshanks mice are substantially farther in morphospace from unselected groups than the latter are from each other (mean Euclidean distances 0.017 vs 0.010, Supplementary Table S6)

*Intergenerational changes occurred in a stepwise process*

F09 LS1 and LS2 score more positively along PC1 in the same direction as F20 LS1 and LS2 after removing size effects (Figures 1B, 2). In other words, F09 LS1 and LS2 appear to have intermediate shapes along PC1 between F01 groups and F20 selected lines (Figure 2). This led us to ask how intergenerational changes in cranium shape occurred throughout the selection process. We computed the mean shapes of LS1 and LS2 lines over time and compared them using deformation heat maps to track shape change between generations within a selection line. Our results show that indirect responses to selection in the Longshanks cranium occurred in a stepwise process: shape change in the first nine generations of selection contributed to the reduction in vault height, whereas the remaining 11 generations of tibia selection led to a reduction in cranial width at the zygomatic arches in parallel with snout elongation (arrows in Figure 2). In comparison, intergenerational changes in the Control lines shows virtually no change in cranial vault height between F01 and F09, and a reduction in the occipital area of the cranium from F09 to F20 (Figure 2).

bioRxiv preprint doi: https://doi.org/10.1101/2020.10.01.321604; this version posted October 1, 2020. The copyright holder for this preprint (which was not certified by peer review) is the author/funder, who has granted bioRxiv a license to display the preprint in perpetuity. It is made available under aCC-BY-NC-ND 4.0 International license.

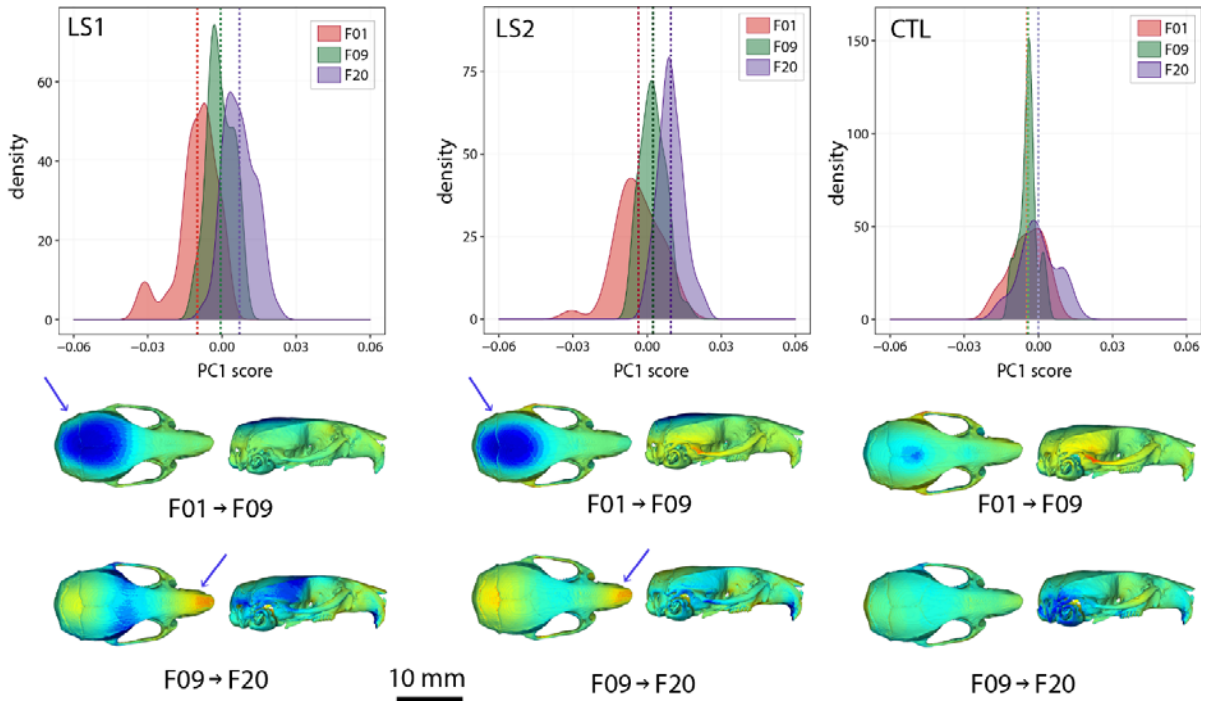


**Figure 2** - Intergenerational shape changes within both Longshanks lines and Controls throughout the selection process. Top: Density plots following intergenerational shifts in mean PC1 scores within LS1 (left), LS2 (center), and CTL (right) lines for size and sex adjusted shape data. Bottom: Heatmaps showing shape transformations between mean shapes in the first 9 generations of selection (F01 to F09) and the next 11 generations (F09 to F20) after correcting for size and sex effects. Blue indicates areas of relative reduction, red indicates areas of relative expansion, and green indicates neutral areas. Longshanks

bioRxiv preprint doi: https://doi.org/10.1101/2020.10.01.321604; this version posted October 1, 2020. The copyright holder for this preprint (which was not certified by peer review) is the author/funder, who has granted bioRxiv a license to display the preprint in perpetuity. It is made available under aCC-BY-NC-ND 4.0 International license.

## Longshanks P07 Neonates

*Neonate crania have similar shape patterns as Longshanks adults*

We investigated if we could detect the adult pattern in shape differences earlier in ontogeny. Using one-week old (P07) Longshanks neonates, we compared cranial shape at a time when the Longshanks tibia is growing most rapidly and tibia length differences are already observable (Farooq *et al.*, 2017; Marchini and Rolian, 2018) (Supplementary Figure S5, Supplementary Table S4). After regressing out litter size effects, our PCA of neonate cranial shape showed a large separation in morphospace between the selected lines and Controls (Figure 3). LS1 and LS2 cluster more closely than Controls and have skulls that are longer, narrower and have reduced vault heights (Figures 3, 4). The Procrustes ANCOVA and pairwise comparisons showed that LS1, LS2 and Control neonates significantly differ from each other in cranium shape. In addition, we observed via deformation heatmaps that the cranial pattern seen in Longshanks adults exists by one-week post partum and becomes more marked with age (Figure 4). The LS2 selection replicate appears to have reduced magnitudes of cranial response compared to LS1 at F20 and in neonates (Figures 1B, 2, 4).

*Longshanks neonate cranial bases are flatter than Controls and differ in synchondrosis shape*

Given the underlying developmental relationship between the cranial base and the long bones, we asked if the neonate cranial bases differed in shape along the sagittal plane between Longshanks and Controls, where the synchondroses' primary axis of elongation exists. We performed a 2D morphometric analysis and found that groups differed in cranial base shape after removing litter size effects ($F = 20.972$, $p < 0.001$). As with the neonate cranial form, Procrustes

bioRxiv preprint doi: https://doi.org/10.1101/2020.10.01.321604; this version posted October 1, 2020. The copyright holder for this preprint (which was not certified by peer review) is the author/funder, who has granted bioRxiv a license to display the preprint in perpetuity. It is made available under aCC-BY-NC-ND 4.0 International license.

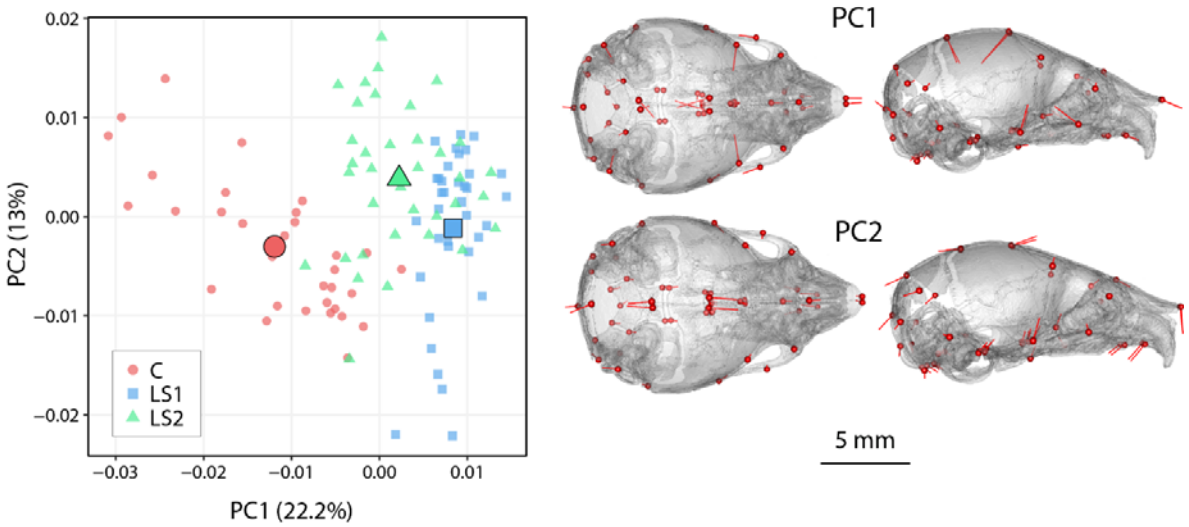


**Figure 3** - Scatter plots of the first principal components (PC) in neonate Longshanks and Control cranium Procrustes shape variables at generation 32 (F32). Left: Plot of litter size adjusted Procrustes shape variables (left), large symbols indicate mean PC1 and PC2 scores for each respective cohort. Shapes of individual points indicate Longshanks lines (circle = CTL, square = LS1, and triangle = LS2). Right: Neonate cranium with vectors of shape change at each cranium landmark (magnified 4 times for visualization) showing shape transformations along PC1 (top) and along PC2 (bottom) from negative to positive scores.

ANCOVA and pairwise comparisons of cranial base shape showed that LS1, LS2 and Control neonate mean cranial shapes all differ from each other. Longshanks neonate cranial base shapes differed from Controls in a similar pattern, but to different extents, with LS2 assuming an intermediate position in cranial base morphospace (Figure 5A). Deformations comparing a mean Control cranial base to LS1 and LS2 means show a flattening of the cranial base in both Longshanks lines (Figure 5B). Moreover, the shape of the ISS changes in LS1 and LS2 compared to Controls, expanding dorsally to become more wedge-shaped, whereas the SOS shows no significant shape change differentiating them from the Control SOS shape (Figure 5B). This suggests that a cellular change in the dorsal aspect of the ISS could be driving cranial base

bioRxiv preprint doi: https://doi.org/10.1101/2020.10.01.321604; this version posted October 1, 2020. The copyright holder for this preprint (which was not certified by peer review) is the author/funder, who has granted bioRxiv a license to display the preprint in perpetuity. It is made available under aCC-BY-NC-ND 4.0 International license.

flattening in the Longshanks juvenile skull, and hence potentially into adulthood given the broadly similar shape changes observed at both stages.

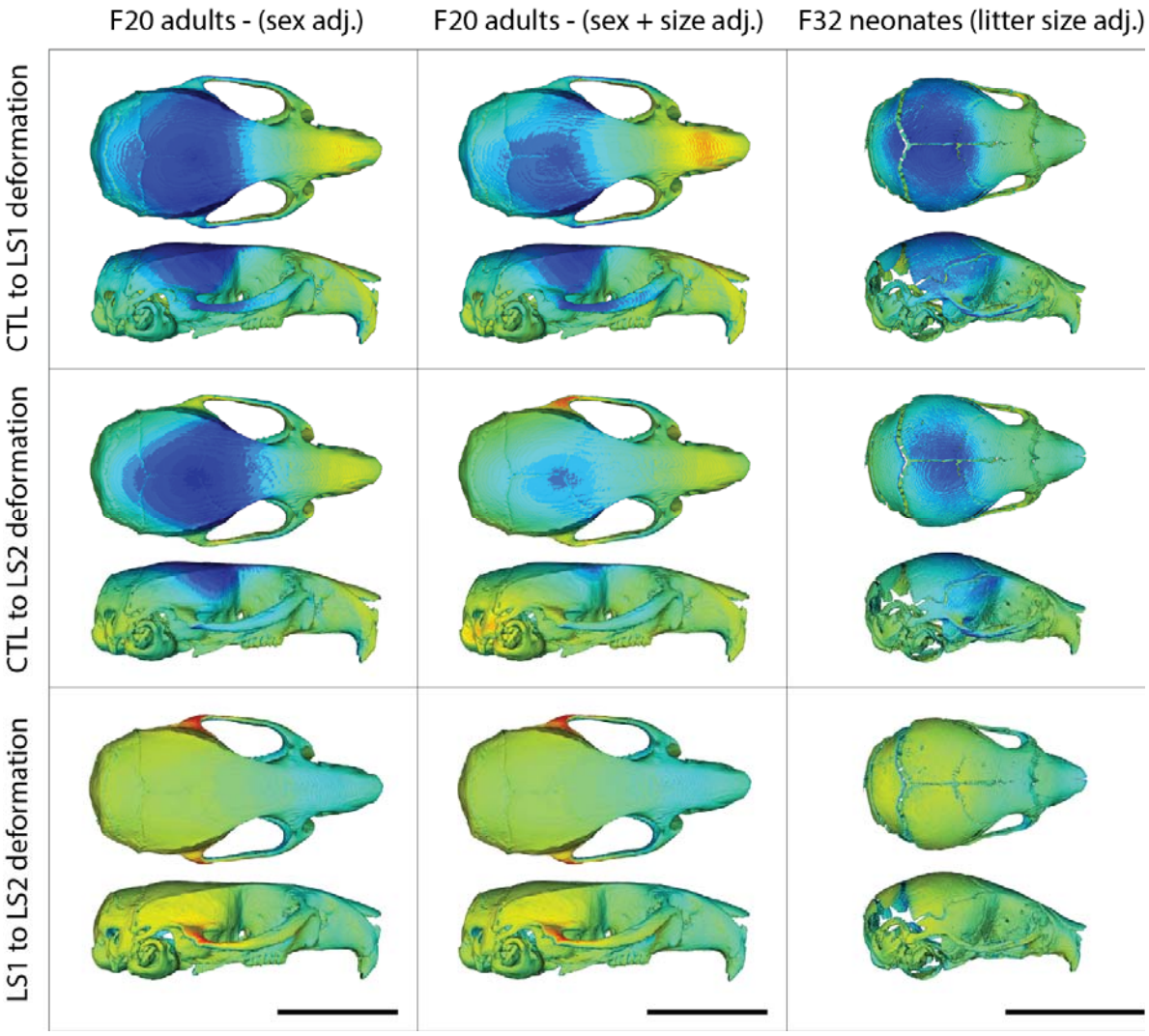


**Figure 4** – Comparison of adult and neonate cranial phenotypes through shape change heatmaps. Heatmaps show the deformations required to transform between the mean shape of a given cohort to the mean shape of another. Blue indicates areas of relative reduction, red indicates areas of relative expansion, and green indicates neutral areas. Scale bar = 10 mm.

bioRxiv preprint doi: https://doi.org/10.1101/2020.10.01.321604; this version posted October 1, 2020. The copyright holder for this preprint (which was not certified by peer review) is the author/funder, who has granted bioRxiv a license to display the preprint in perpetuity. It is made available under aCC-BY-NC-ND 4.0 International license.

To qualitatively validate the cellular changes inferred from our 2D GM analysis, we collected and imaged cranial base sections near the sagittal midline. Since these developmental shape differences are still subtle, we selected two representative extreme specimens that had large differences in ossified tibia length, cranial base shape and cranium shape, yet comparable cranium centroid sizes so that size would not confound our analysis. In agreement with our morphometric data, the SOS does not differ qualitatively between these extreme specimens (Figure 5C). However, the ISS is markedly larger in our Longshanks specimen compared to the Control, with larger resting and proliferative zones that recapitulate the cellular differences characterized in the Longshanks epiphysis (Figure 5C) (Marchini and Rolian, 2018). Crucially, the ISS is more wedge-shaped in our Longshanks specimen at the cellular level, supporting the observed ISS changes at the morphometric level (Figure 5B, C).

bioRxiv preprint doi: https://doi.org/10.1101/2020.10.01.321604; this version posted October 1, 2020. The copyright holder for this preprint (which was not certified by peer review) is the author/funder, who has granted bioRxiv a license to display the preprint in perpetuity. It is made available under aCC-BY-NC-ND 4.0 International license.

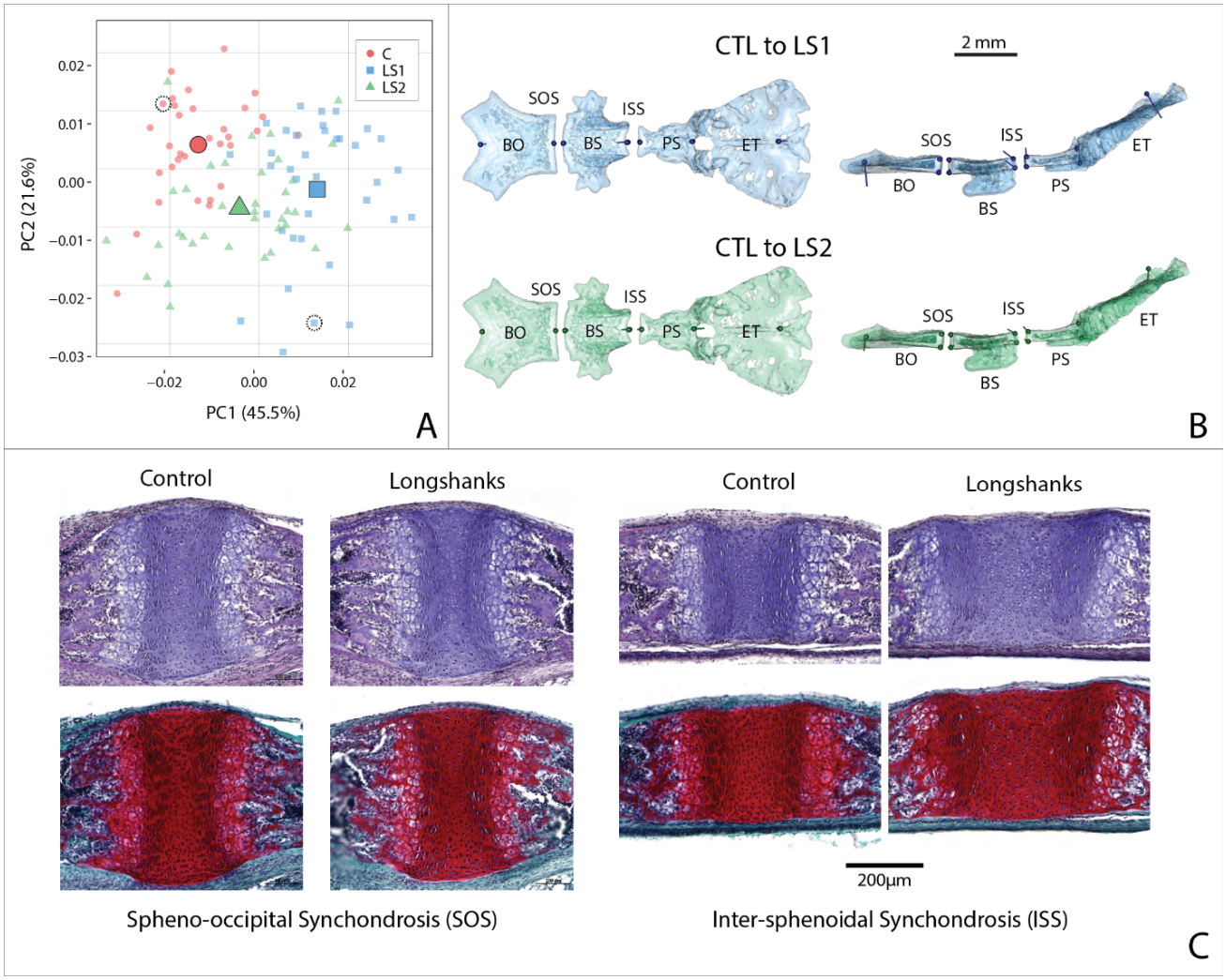


**Figure 5** - Cranial base contribution to the Longshanks phenotype. (A) Scatter plot of the first two PCs of litter size-adjusted Longshanks and Control cranial base Procrustes shape variables in generation 32 (F32) neonates. Large symbols indicate mean PC1 and PC2 scores for each respective cohort. (B) Neonate cranial bases with vectors of shape change at midline cranial base landmarks (magnified 6 times for visualization) showing shape transformations to go from the mean Control cranial base to the mean LS1 (blue) and mean LS2 (green) cranial base shapes. Views in (B) are dorsal (left) and lateral (right). Abbreviations: basi-occipital bone (BO), spheno-occipital synchondrosis (SOS), basi-sphenoid bone (BS), intersphenoidal synchondrosis (ISS), presphenoid bone (PS) and ethmoid (ET). (C) Sagittal midline histological sections stained in H+E (top) and safranin-o (bottom) showing differences in synchondrosis morphology of two extreme specimens in CTL and LS1 of approximately equal centroid size (indicated by dashed circles in A).

370

bioRxiv preprint doi: https://doi.org/10.1101/2020.10.01.321604; this version posted October 1, 2020. The copyright holder for this preprint (which was not certified by peer review) is the author/funder, who has granted bioRxiv a license to display the preprint in perpetuity. It is made available under aCC-BY-NC-ND 4.0 International license.

## Discussion

We investigated correlated evolution between the limb and cranium in the selectively bred Longshanks mouse. Our morphometric analysis of adult cranium shape demonstrated that 20 generations of selection for longer tibiae relative to body mass are associated with the elongation of the cranium along the rostral caudal axis in Longshanks mice, independent of an overall increase in cranial size (Figure 1). In parallel, the cranium of Longshanks decreased in width between the zygomatic arches and reduced in vault height at the bregma and lambda (Figure 1). LS2 mice appear to have a more subtle phenotype than LS1 in adulthood and at P07 (Figures 1, 2, 4, 6A). This is not unexpected, as other genomic and phenotypic differences in the response to selection between LS1 and LS2 have been documented previously (Farooq *et al.*, 2017; Castro *et al.*, 2019; Cosman, Britz and Rolian, 2019).

The magnitudes of cranial shape change remain small in Longshanks relative to Controls, in comparison to stark morphological differences seen in skeletal mouse mutants (Munroe *et al.*, 2009; Gong, 2012; Holmes, 2012). However, in this study, we are more interested in patterns of shape change rather than magnitudes of change. Over 20 generations, the main target of selection, the tibia, increased in length by just 15%. As such, it is expected that secondary cranial shape changes, while potentially significant in terms of long-term evolution, will be quite subtle. Moreover, selection in the tibia appears to have increased the variation in cranium measures, such as centroid size and cranial shape (Figures 2, S6). While the F20 LS1 and LS2 samples have new extreme cranium shapes not seen in earlier generations, their effects on the mean shape are dampened substantially by the fact that many F20 mice still have crania that resemble F01 unselected mice.

bioRxiv preprint doi: https://doi.org/10.1101/2020.10.01.321604; this version posted October 1, 2020. The copyright holder for this preprint (which was not certified by peer review) is the author/funder, who has granted bioRxiv a license to display the preprint in perpetuity. It is made available under aCC-BY-NC-ND 4.0 International license.

The net cranium phenotypic change manifested as a stepwise series of two evolutionary shape changes rather than changes that occurred in concert. The cranium of both selected lines consistently reduced in vault height in the first nine generations of tibia selection and then elongated and narrowed in the next eleven generations of selection (Figure 2). In comparison, the Control line shows cranial shape changes around the zygomatic and occipital regions, which are presumably due to stochastic intergenerational variation in the Control line (i.e., drift), and/or to sampling artifacts, such as low sample size and family diversity in F09 Controls (Table 1). Stepwise mechanisms of evolutionary change have also been described in natural populations. Parmenter and colleagues noted that Gough Island mice, which differ significantly in body size compared to mainland relatives, have crania that are longer and narrower, without differences in vault height (Parmenter *et al.*, 2016). These shape differences coincide with the intergenerational changes described in the F09 to F20 Longshanks shape trajectory, highlighting the power of selection experiments to uncover the tempo and mode of evolutionary change across multiple traits.

The two sets of shape changes may reflect the way selection targeted sources of variation in Longshanks. Strong selection pressure may have targeted processes that drive the generation of local tibia length variation which are also correlated to the cranial base development via pleiotropy. In a recent paper investigating the underlying genomics of Longshanks, we highlighted an allelic variant that reduces expression of NKX-3.2, a bone growth repressor, that was brought to near-fixation by generation 17 in both Longshanks lines in parallel (Castro *et al.*, 2019). Interestingly, complete ablation of *nkx-3.2* (also known as bagpipe-1) results in cranial base truncation and premature synchondrosis fusion in mice (Lettice *et al.*, 1999). Thus, it is

bioRxiv preprint doi: https://doi.org/10.1101/2020.10.01.321604; this version posted October 1, 2020. The copyright holder for this preprint (which was not certified by peer review) is the author/funder, who has granted bioRxiv a license to display the preprint in perpetuity. It is made available under aCC-BY-NC-ND 4.0 International license.

possible that selection for increased tibia growth via *nkx-3.2* downregulation caused indirect cranial changes through the pleiotropic effects of *nkx-3.2*.

The second set of cranium shape changes may reflect a shift to selection targeting processes that generate systemic skeletal size variation following depletion or reduction of local allelic variation contributing to tibia length. Several factors could cause a systemic increase in growth of the Longshanks skeleton, such as altered expression of factors that modulate the IHH-PTHrP axis systemically in all growth plates or a bone tissue specific increase to the sensitivity to endocrine factors. A shift in the target of selection from genes of local effect to systemic effects could explain the skeletal increases in the entire post-cranium of Longshanks mice and would agree with our present findings that the allometric scaling of cranium size to body mass has been altered in Longshanks (Sparrow *et al.*, 2017).

Our investigation of Longshanks neonate ontogeny revealed that the adult cranium pattern is already present by one-week post partum (Figure 4). Analyses of cranial base shape in P07 neonates reveals that the cranial base is flatter in Longshanks mice at this time (Figure 5). Moreover, 2D morphometrics at the midline and histology demonstrated that Longshanks neonates have a larger ISS with larger resting and proliferative zones, especially in its dorsal aspect (Figure 5B, C), much like differences characterized in the tibial proximal epiphysis of Longshanks (Marchini and Rolian, 2018). These results suggest that the ISS responded to selection on the tibia independently of the SOS and may be responsible in part for the Longshanks cranial phenotype. We note, however, that our ontogenetic analysis captures only one developmental stage and that the apparent uncoupling of the synchondroses may be because the SOS has developmentally important differences in Longshanks at a different time in development (Wealthall and Herring, 2006).

bioRxiv preprint doi: https://doi.org/10.1101/2020.10.01.321604; this version posted October 1, 2020. The copyright holder for this preprint (which was not certified by peer review) is the author/funder, who has granted bioRxiv a license to display the preprint in perpetuity. It is made available under aCC-BY-NC-ND 4.0 International license.

Differential timing of SOS and ISS fusion are widespread across clades, suggesting these growth centers are partly under independent genetic and developmental control. For example, in humans, the ISS begins fusing at birth, whereas the SOS does not fuse until adolescence (Madeline and Elster, 1995). In domestic dogs, premature fusion of the SOS is a prominent feature of brachycephalic dogs (Schmidt *et al.*, 2013). Moreover, knock-out studies of skeletogenic factors in rodents have noted concerted changes in the postcranial epiphyses and synchondroses, but both synchondroses do not always respond to these perturbations in similar manners (reviewed in (Vora, 2017)). For example, in mice, Indian hedgehog ($Ihh^{-/-}$) knockout results in significantly more ectopic hypertrophic chondrocytes in the ISS than in the SOS (Young *et al.*, 2006).

Intrinsic genetic regulatory differences may stem from the fact that the two synchondroses have distinct embryonic origins. The pre-sphenoid and basi-sphenoid bones originate from neural crest cells that commit to endochondral ossification, whereas the basi-occiptal bone forms from mesenchymal condensations of prechordal mesoderm (McBratney-Owen *et al.*, 2008; Richtsmeier and Flaherty, 2013). The SOS and ISS also develop in proximity of different tissues with potentially different signalling influences, for example, the future SOS grows directly below the developing pituitary gland (McBratney-Owen *et al.*, 2008). The respective synchondroses have different mineralization patterns in both C57BL/6J and CD-1 mice that are likely indicative of independent regulation resulting from differences in embryonic tissue origin (Wealthall and Herring, 2006; Vora, Camci and Cox, 2016). These developmental differences may account for some of the differences observed between Longshanks and Control.

Extensive work has gone into understanding integration and epigenetic interactions within the mammalian cranium (DE, CF and MJ, 2000; Bookstein *et al.*, 2003; Goswami, 2006; Goswami

bioRxiv preprint doi: https://doi.org/10.1101/2020.10.01.321604; this version posted October 1, 2020. The copyright holder for this preprint (which was not certified by peer review) is the author/funder, who has granted bioRxiv a license to display the preprint in perpetuity. It is made available under aCC-BY-NC-ND 4.0 International license.

*et al.*, 2012; Singh *et al.*, 2012; Bastir and Rosas, 2016; Neaux, 2016; Neaux *et al.*, 2019). Previous studies have divided the skull into three independently variable regions (i.e. modules), the basicranium, calvarium and the viscerocranium, which differ in embryonic origin and interact at the physical and molecular level to form an integrated complex (Cheverud, 1982, 1996; Goswami, 2006; Martínez-Abadías *et al.*, 2009; Parsons *et al.*, 2011). For example, direct basicranium perturbations by genetic mutation resulting in overgrowth and undergrowth of the basicranium generated predictable shape changes (Parsons *et al.*, 2015). Undergrowth models resulted in shortened faces and tall, domed calvaria whereas overgrowth models, such as the Pten $^{-/-}$ mouse, resulted in flattened calvaria, elongated faces and reduced cranial width (Ford-Hutchinson *et al.*, 2007; Parsons *et al.*, 2015). Moreover, analysis of mutant mouse models affecting brain size and cranial base length demonstrated that the angle of the cranial base is related to brain size, cranial base length and face size (Ross and Ravosa, 1993; Lieberman *et al.*, 2008).

Combining our findings with these studies, we propose a model that relates neonate ontogeny to the adult Longshanks cranium phenotype (Figure 6). We propose that underlying genetic and developmental integration between the developing limb and synchondroses results in correlated cellular changes to the epiphyseal growth plate in the tibia and the ISS in developing Longshanks mice. The enlargement of the ISS would then drive mechanical interaction between the developing basicranial bones that results in a relative flattening of the cranial base and extension of the angle formed between the basicranium and the slope of the ethmoid (Figure 6A). This flattening would result in a commensurate increase in endocranial volume. We do not yet know how the brain volume of Longshanks mice compares to Controls; however, the observed

bioRxiv preprint doi: https://doi.org/10.1101/2020.10.01.321604; this version posted October 1, 2020. The copyright holder for this preprint (which was not certified by peer review) is the author/funder, who has granted bioRxiv a license to display the preprint in perpetuity. It is made available under aCC-BY-NC-ND 4.0 International license.

reduction in vault height and mediolateral width may compensate for cranial base shape changes such that endocranial volume remains constant (Figure 6C).

Lastly, we hypothesize that extension of the cranial base exerts an epigenetic pressure on the developing face that results in snout elongation (Figure 6B). This could be due to mechanical pressure placed on the nasal septum. The interaction between the cranial base and nasal septum, which form a continuous structure running the length of the skull, becomes prominent in post-partum growth (Wealthall and Herring, 2006). Here, expansion of the septo-ethmoidal and septo-presphenoidal junctions contributes to the out-growth of the murine face (Wealthall and Herring, 2006). The nasal septum is physically linked to the maxilla and rostral tip of the nasal bones by ligaments, and resection of these ligaments leads to reduced facial growth and decreased nasofrontal suture expansion in rats and mice, respectively (Latham, 1970; Gange and Johnston, 1974; Siegel *et al.*, 1985). Thus, it is possible that the enlarged ISS confers a mechanical pressure onto the nasal septum via the septo-prepshenoidal and septo-ethmoidal junctions, which then

bioRxiv preprint doi: https://doi.org/10.1101/2020.10.01.321604; this version posted October 1, 2020. The copyright holder for this preprint (which was not certified by peer review) is the author/funder, who has granted bioRxiv a license to display the preprint in perpetuity. It is made available under aCC-BY-NC-ND 4.0 International license.

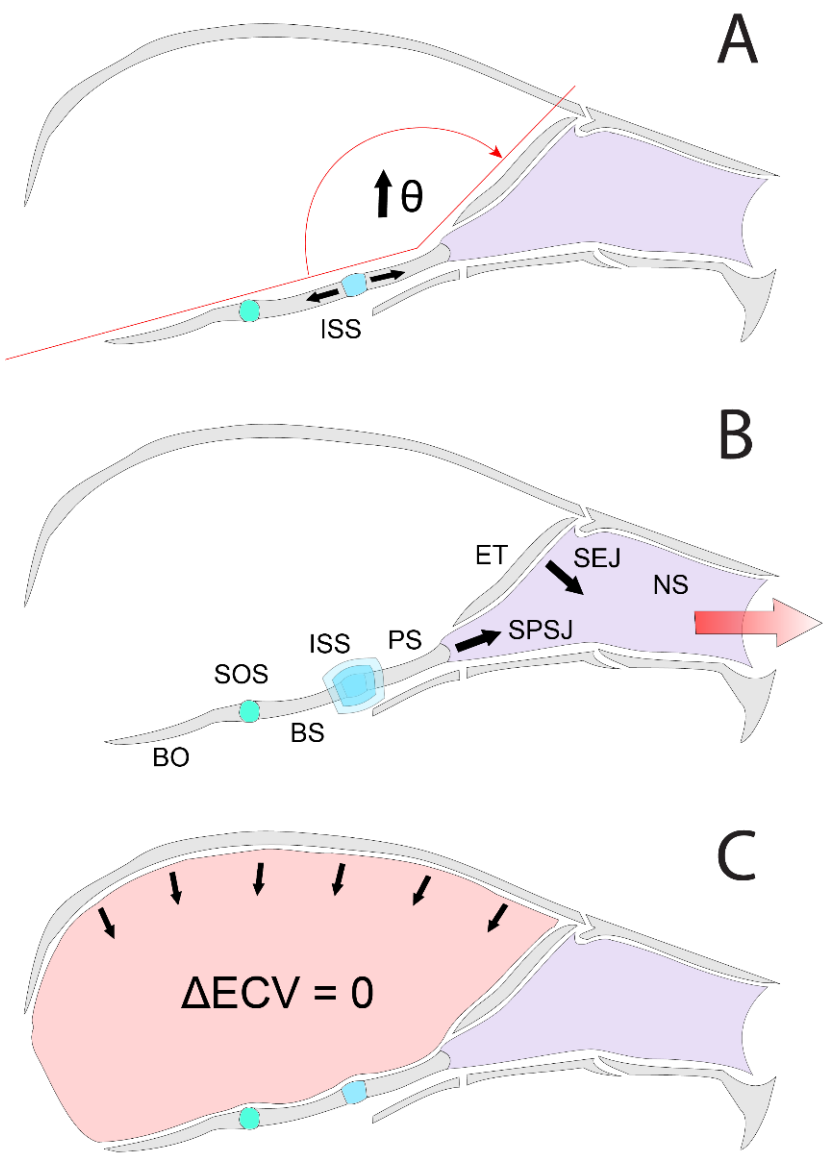


**Figure 6** – Model relating the Longshanks neonate phenotypes to the adult cranial form. (A) Intersphenoidal synchondrosis (blue) expansion drives cranial base flattening (extension of theta). The spheno-occipital synchondrosis remains unchanged (green). (B) Intersphenoidal synchondrosis expansion places mechanical pressure (black arrows) on the nasal septum (purple) that enhances facial outgrowth (red arrow). (C) Vault height reduces (black arrows) to compensate for the effect of cranial base flattening on endocranial volume (red). Endocranial volume (ECV), basi-occipital bone (BO), spheno-occipital synchondrosis (SOS), basi-sphenoid bone (BS), intersphenoidal synchondrosis (ISS), presphenoid bone (PS), ethmoid (ET), nasal septum (NS), septo-ethmoidal junction (SEJ) and septo-presphenoidal junction (SPSJ).

bioRxiv preprint doi: https://doi.org/10.1101/2020.10.01.321604; this version posted October 1, 2020. The copyright holder for this preprint (which was not certified by peer review) is the author/funder, who has granted bioRxiv a license to display the preprint in perpetuity. It is made available under aCC-BY-NC-ND 4.0 International license.

the surrounding facial bones. In line with this idea, mice lacking an ethmoid via *Foxl2* ablation have reduced face size with small maxillary, premaxillary, and nasal bones (Marongiu *et al.*, 2015).

In this study, we characterized secondary skeletal responses to tibia selection that likely arose due to shared underlying genetic and developmental mechanisms between the cranium and tibia, specifically endochondral ossification. The limb and cranium are often considered separate modules in morphological analyses (Young and Hallgrímsson, 2005). Our results highlight the importance of considering evolution of the skeleton as a whole. Our study shows how indirect, and potentially non-adaptive, skeletal changes can occur due to genetic and/or developmental overlap among physically and functionally distant body parts. These findings have implications for how we reconstruct skeletal evolutionary histories of extant and extinct mammalian lineages by providing empirical evidence of the existence of skeletal traits that arise solely as side effects of selection acting elsewhere.

## Limitations and Future Directions

We propose that changes to cranial form occurred as non-adaptive, secondary effects from selection for increased tibia length. We cannot say with certainty, however, that there were no selective pressures acting on the cranium. If selected Longshanks breeders consistently had larger craniums at all times during the experiment, then we cannot rule out the possibility that cranium form, which was not quantified when selecting breeders, had an effect on their fitness, which would make cranial shape change adaptive. We note, however, that the phenotypic correlation between cranial shape and tibia length within generations is weak, suggesting that

bioRxiv preprint doi: https://doi.org/10.1101/2020.10.01.321604; this version posted October 1, 2020. The copyright holder for this preprint (which was not certified by peer review) is the author/funder, who has granted bioRxiv a license to display the preprint in perpetuity. It is made available under aCC-BY-NC-ND 4.0 International license.

selecting for longer tibiae did not necessarily mean selecting for altered cranial shape/size in this experiment (Figure S8), and that any correlated response in cranial shape is thus more likely due to underlying genetic correlations. Future works will seek to investigate cranial base shape and synchondrosis cellular architecture at other timepoints in ontogeny, e.g., reaching as far back as E11-E16 when the chondrocranium forms in utero (McBratney-Owen *et al.*, 2008). Quantitative histomorphometry of the synchondroses will also be necessary to verify our qualitative assessment of the size of the respective chondrocyte zones observed in our sample of phenotypic extremes.

## Acknowledgments

The authors are grateful to the Animal Resource Center staff at the University of Calgary for the continued care they provide to the Longshanks colonies. The authors are also indebted to Jason Anderson and Jessica Theodor for granting access to the SkyScan 1173 uCT scanner for data acquisition. The authors are also grateful to Dragana Ponjevic for expertise in histology and Heather Jamniczky for guidance in data analysis. This work was supported by a Natural Sciences and Engineering Research Council Canada Graduate Scholarships – Master's award to CMU, a Natural Sciences and Engineering Research Council Discovery Grant 4181932 to CR, and the Faculty of Veterinary Medicine at the University of Calgary (www.vet.ucalgary.ca).

## Competing Interests

The authors declare no conflict of interest.

bioRxiv preprint doi: https://doi.org/10.1101/2020.10.01.321604; this version posted October 1, 2020. The copyright holder for this preprint (which was not certified by peer review) is the author/funder, who has granted bioRxiv a license to display the preprint in perpetuity. It is made available under aCC-BY-NC-ND 4.0 International license.

## References

Adams, D., Collyer, M. and Kaliontzopoulou, A. (2020) 'Geomorph: Software for geometric morphometric analyses. R package version 3.2.1.' Available at: https://cran.r-project.org/package=geomorph.

Armbruster, W. S. and Schwaegerle, K. E. (1996) 'Causes of covariation of phenotypic traits among populations', *Journal of Evolutionary Biology*, 9(3), pp. 261–276. doi: 10.1046/j.1420-9101.1996.9030261.x.

Avants, B. B. *et al.* (2011) 'A reproducible evaluation of ANTs similarity metric performance in brain image registration', *NeuroImage*, 54(3), pp. 2033–2044. doi: 10.1016/j.neuroimage.2010.09.025.

Bastir, M. and Rosas, A. (2006) 'Correlated variation between the lateral basicranium and the face: A geometric morphometric study in different human groups', *Archives of Oral Biology*, 51(9), pp. 814–824. doi: 10.1016/j.archoralbio.2006.03.009.

Bastir, M. and Rosas, A. (2016) 'Cranial base topology and basic trends in the facial evolution of Homo', *Journal of Human Evolution*, 91, pp. 26–35. doi: 10.1016/j.jhevol.2015.11.001.

De Beer, G. (1937) *The development of the vertebrate skull*. Oxford: The Clarendon Press.

Bookstein, F. L. *et al.* (2003) 'Cranial integration in Homo: Singular warps analysis of the midsagittal plane in ontogeny and evolution', *Journal of Human Evolution*, 44(2), pp. 167–187. doi: 10.1016/S0047-2484(02)00201-4.

Castro, J. P. *et al.* (2019) 'An integrative genomic analysis of the Longshanks selection experiment for longer limbs in mice', *eLife*, 8. doi: 10.7554/elife.42014.

bioRxiv preprint doi: https://doi.org/10.1101/2020.10.01.321604; this version posted October 1, 2020. The copyright holder for this preprint (which was not certified by peer review) is the author/funder, who has granted bioRxiv a license to display the preprint in perpetuity. It is made available under aCC-BY-NC-ND 4.0 International license.

Cheverud, J. M. (1982) 'Relationships among ontogenetic, static, and evolutionary allometry', *American Journal of Physical Anthropology*, 59(2), pp. 139–149. doi: 10.1002/ajpa.1330590204.

Cheverud, J. M. (1996) 'Developmental integration and the evolution of pleiotropyl', *American Zoologist*, 36(1), pp. 44–50. doi: 10.1093/icb/36.1.44.

Collyer, M. L. and Adams, D. C. (2018) 'RRPP: An R package for fitting linear models to high-dimensional data using residual randomization', *Methods in Ecology and Evolution*. Edited by R. Freckleton, 9(7), pp. 1772–1779. doi: 10.1111/2041-210X.13029.

Collyer, M. L., Sekora, D. J. and Adams, D. C. (2015) 'A method for analysis of phenotypic change for phenotypes described by high-dimensional data', *Heredity*, 115(4), pp. 357–365. doi: 10.1038/hdy.2014.75.

Cosman, M. N., Britz, H. M. and Rolian, C. (2019) 'Selection for longer limbs in mice increases bone stiffness and brittleness, but does not alter bending strength', *Journal of Experimental Biology*, 222(9). doi: 10.1242/jeb.203125.

Cosman, M. N., Sparrow, L. M. and Rolian, C. (2016) 'Changes in shape and cross-sectional geometry in the tibia of mice selectively bred for increases in relative bone length', *Journal of Anatomy*, 228(6), pp. 940–951. doi: 10.1111/joa.12459.

von Cramon-Taubadel, N. (2019) 'Multivariate morphometrics, quantitative genetics, and neutral theory: Developing a "modern synthesis" for primate evolutionary morphology', *Evolutionary Anthropology: Issues, News, and Reviews*, 28(1), pp. 21–33. doi: 10.1002/evan.21761.

DE, L., CF, R. and MJ, R. (2000) 'The primate cranial base: ontogeny, function, and

bioRxiv preprint doi: https://doi.org/10.1101/2020.10.01.321604; this version posted October 1, 2020. The copyright holder for this preprint (which was not certified by peer review) is the author/funder, who has granted bioRxiv a license to display the preprint in perpetuity. It is made available under aCC-BY-NC-ND 4.0 International license.

integration', *American journal of physical anthropology*, Suppl 31. doi: 10.1002/1096-8644(2000)43:31+<117::AID-AJPA5>3.3.CO;2-9.

Devine, J. *et al.* (2020) 'A Registration and Deep Learning Approach to Automated Landmark Detection for Geometric Morphometrics', *Evolutionary Biology*, 47(3), pp. 246–259. doi: 10.1007/s11692-020-09508-8.

Farooq, S. *et al.* (2017) 'Cortical and trabecular morphology is altered in the limb bones of mice artificially selected for faster skeletal growth', *Scientific Reports*, 7(1), pp. 10527–10527. doi: 10.1038/s41598-017-10317-x.

Ford-Hutchinson, A. F. *et al.* (2007) 'Inactivation of Pten in Osteo-Chondroprogenitor Cells Leads to Epiphyseal Growth Plate Abnormalities and Skeletal Overgrowth', *Journal of Bone and Mineral Research*, 22(8), pp. 1245–1259. doi: 10.1359/jbmr.070420.

Fruciano, C. (2016) 'Measurement error in geometric morphometrics', *Development Genes and Evolution*. Springer Verlag, pp. 139–158. doi: 10.1007/s00427-016-0537-4.

Gange, R. J. and Johnston, L. E. (1974) 'The septopremaxillary attachment and midfacial growth. An experimental study on the albino rat', *American Journal of Orthodontics*, 66(1), pp. 71–81. doi: 10.1016/0002-9416(74)90194-8.

Gong, S. G. (2012) 'The Fgfr2 W290R mouse model of Crouzon syndrome', *Child's Nervous System*, 28(9), pp. 1495–1503. doi: 10.1007/s00381-012-1792-y.

Goodall, C. (1991) 'Procrustes Methods in the Statistical Analysis of Shape', *Journal of the Royal Statistical Society: Series B (Methodological)*, 53(2), pp. 285–321. doi: 10.1111/j.2517-6161.1991.tb01825.x.

bioRxiv preprint doi: https://doi.org/10.1101/2020.10.01.321604; this version posted October 1, 2020. The copyright holder for this preprint (which was not certified by peer review) is the author/funder, who has granted bioRxiv a license to display the preprint in perpetuity. It is made available under aCC-BY-NC-ND 4.0 International license.

Goswami, A. (2006) 'Morphological Integration in the Carnivoran Skull', *Evolution*, 60(1), pp. 169–183. doi: 10.1111/j.0014-3820.2006.tb01091.x.

Goswami, A. *et al.* (2012) 'Shape, variance and integration during craniogenesis: contrasting marsupial and placental mammals', *Journal of Evolutionary Biology*, 25(5), pp. 862–872. doi: 10.1111/j.1420-9101.2012.02477.x.

Gould, S. J. and Lewontin, R. C. (1979) 'The spandrels of San Marco and the Panglossian paradigm: a critique of the adaptationist programme', *Proceedings of the Royal Society of London. Series B. Biological Sciences*, 205(1161), pp. 581–598. doi: 10.1098/rspb.1979.0086.

Hallgrímsson, B. *et al.* (2009) 'Deciphering the palimpsest: Studying the relationship between morphological integration and phenotypic covariation', *Evolutionary Biology*, 36(4), pp. 355–376. doi: 10.1007/s11692-009-9076-5.

Hallgrímsson, B. and Hall, B. K. (2005) 'Variation and variability: Central concepts in biology', in *Variation*. Elsevier Inc., pp. 1–7. doi: 10.1016/B978-012088777-4/50003-X.

Hallgrímsson, B. and Lieberman, D. E. (2008) 'Mouse models and the evolutionary developmental biology of the skull', *Integrative and Comparative Biology*, 48(3), pp. 373–384. doi: 10.1093/icb/icn076.

Hendrikse, J. L., Parsons, T. E. and Hallgrímsson, B. (2007) 'Evolvability as the proper focus of evolutionary developmental biology', *Evolution and Development*, 9(4), pp. 393–401. doi: 10.1111/j.1525-142X.2007.00176.x.

Holmes, G. (2012) 'Mouse models of Apert syndrome', *Child's Nervous System*, 28(9), pp. 1505–1510. doi: 10.1007/s00381-012-1872-z.

bioRxiv preprint doi: https://doi.org/10.1101/2020.10.01.321604; this version posted October 1, 2020. The copyright holder for this preprint (which was not certified by peer review) is the author/funder, who has granted bioRxiv a license to display the preprint in perpetuity. It is made available under aCC-BY-NC-ND 4.0 International license.

Karp, N. A. *et al.* (2017) 'Prevalence of sexual dimorphism in mammalian phenotypic traits', *Nature Communications*, 8(1), p. 21. doi: 10.1038/ncomms15475.

Klingenberg, C. P. (2016) 'Size, shape, and form: concepts of allometry in geometric morphometrics', *Development Genes and Evolution*. Springer Verlag, pp. 113–137. doi: 10.1007/s00427-016-0539-2.

Kronenberg, H. M. (2003) 'Developmental regulation of the growth plate', *Nature*. Nature, pp. 332–336. doi: 10.1038/nature01657.

Latham, R. A. (1970) 'Maxillary development and growth: the septo-premaxillary ligament.', *Journal of Anatomy*, 107(3), pp. 471–478. Available at: https://www.ncbi.nlm.nih.gov/pmc/articles/PMC1233872/ (Accessed: 29 September 2020).

Lefebvre, V. and Bhattaram, P. (2010) 'Vertebrate skeletogenesis', in *Current Topics in Developmental Biology*. Academic Press Inc., pp. 291–317. doi: 10.1016/S0070-2153(10)90008-2.

Lerch, J. P., Sled, J. G. and Henkelman, R. M. (2010) 'MRI phenotyping of genetically altered mice', *Methods in Molecular Biology*, 711, pp. 349–361. doi: 10.1007/978-1-61737-992-5_17.

Lettice, L. A. *et al.* (1999) 'The mouse bagpipe gene controls development of axial skeleton, skull, and spleen', *Proceedings of the National Academy of Sciences of the United States of America*, 96(17), pp. 9695–9700. doi: 10.1073/pnas.96.17.9695.

Lieberman, D. E. *et al.* (2008) 'Spatial packing, cranial base angulation, and craniofacial shape variation in the mammalian skull: Testing a new model using mice', *Journal of Anatomy*,

bioRxiv preprint doi: https://doi.org/10.1101/2020.10.01.321604; this version posted October 1, 2020. The copyright holder for this preprint (which was not certified by peer review) is the author/funder, who has granted bioRxiv a license to display the preprint in perpetuity. It is made available under aCC-BY-NC-ND 4.0 International license.

212(6), pp. 720–735. doi: 10.1111/j.1469-7580.2008.00900.x.

Mackie, E. J. *et al.* (2008) 'Endochondral ossification: How cartilage is converted into bone in the developing skeleton', *International Journal of Biochemistry and Cell Biology*. Int J Biochem Cell Biol, pp. 46–62. doi: 10.1016/j.biocel.2007.06.009.

Madeline, L. A. and Elster, A. D. (1995) 'Suture closure in the human chondrocranium: CT assessment', *Radiology*, 196(3), pp. 747–756. doi: 10.1148/radiology.196.3.7644639.

Marchini, M. *et al.* (2014) 'Impacts of genetic correlation on the independent evolution of body mass and skeletal size in mammals', *BMC Evolutionary Biology*, 14(1), p. 258. doi: 10.1186/s12862-014-0258-0.

Marchini, M. and Rolian, C. (2018) 'Artificial selection sheds light on developmental mechanisms of limb elongation', *Evolution*, 72(4), pp. 825–837. doi: 10.1111/evo.13447.

Marongiu, M. *et al.* (2015) 'FOXL2 modulates cartilage, skeletal development and IGF1-dependent growth in mice', *BMC Developmental Biology*, 15(1), p. 27. doi: 10.1186/s12861-015-0072-y.

Martínez-Abadías, N. *et al.* (2009) 'Heritability of human cranial dimensions: Comparing the evolvability of different cranial regions', *Journal of Anatomy*, 214(1), pp. 19–35. doi: 10.1111/j.1469-7580.2008.01015.x.

McBratney-Owen, B. *et al.* (2008) 'Development and tissue origins of the mammalian cranial base', *Developmental Biology*, 322(1), pp. 121–132. doi: 10.1016/j.ydbio.2008.07.016.

Moss, M. L. (1977) 'A functional analysis of fusion of the tibia and fibula in the rat and mouse', *Cells Tissues Organs*, 97(3), pp. 321–332. doi: 10.1159/000144749.

bioRxiv preprint doi: https://doi.org/10.1101/2020.10.01.321604; this version posted October 1, 2020. The copyright holder for this preprint (which was not certified by peer review) is the author/funder, who has granted bioRxiv a license to display the preprint in perpetuity. It is made available under aCC-BY-NC-ND 4.0 International license.

Munroe, R. J. *et al.* (2009) 'Mouse H6 Homeobox 1 (Hmx1) mutations cause cranial abnormalities and reduced body mass', *BMC Developmental Biology*, 9(1), p. 27. doi: 10.1186/1471-213X-9-27.

Murren, C. J. (2012) 'The integrated phenotype', in *Integrative and Comparative Biology*. Integr Comp Biol, pp. 64–76. doi: 10.1093/icb/ics043.

Neaux, D. (2016) 'DomExp: Experimental domestication and skeleton development in captivity View project', *Article in American Journal of Physical Anthropology*. doi: 10.1002/ajpa.23163.

Neaux, D. *et al.* (2019) 'Morphological integration affects the evolution of midline cranial base, lateral basicranium, and face across primates', *American Journal of Physical Anthropology*, 170(1), pp. 37–47. doi: 10.1002/ajpa.23899.

Parmenter, M. D. *et al.* (2016) 'Genetics of skeletal evolution in unusually large mice from gough island', *Genetics*, 204(4), pp. 1559–1572. doi: 10.1534/genetics.116.193805.

Parsons, T. E. *et al.* (2011) 'Epigenetic integration of the developing brain and face', *Developmental Dynamics*, 240(10), pp. 2233–2244. doi: 10.1002/dvdy.22729.

Parsons, T. E. *et al.* (2015) 'Mind the Gap: Genetic Manipulation of Basicranial Growth within Synchondroses Modulates Calvarial and Facial Shape in Mice through Epigenetic Interactions', *PLOS ONE*. Edited by N. Jeffery, 10(2), p. e0118355. doi: 10.1371/journal.pone.0118355.

Percival, C. J. *et al.* (2019) 'The effect of automated landmark identification on morphometric analyses', *Journal of Anatomy*, 234(6), pp. 917–935. doi: 10.1111/joa.12973.

bioRxiv preprint doi: https://doi.org/10.1101/2020.10.01.321604; this version posted October 1, 2020. The copyright holder for this preprint (which was not certified by peer review) is the author/funder, who has granted bioRxiv a license to display the preprint in perpetuity. It is made available under aCC-BY-NC-ND 4.0 International license.

Price, T. and Langen, T. (1992) 'Evolution of correlated characters', *Trends in Ecology and Evolution*. Trends Ecol Evol, pp. 307–310. doi: 10.1016/0169-5347(92)90229-5.

R Core Team (2020) 'R: A Language and environment for statistical computing (R Foundation for Statistical Computing).'

Richtsmeier, J. T. *et al.* (2006) 'Phenotypic integration of neurocranium and brain', *Journal of Experimental Zoology Part B: Molecular and Developmental Evolution*, 306(4), pp. 360–378. doi: 10.1002/jez.b.21092.

Richtsmeier, J. T. and Flaherty, K. (2013) 'Hand in glove: Brain and skull in development and dysmorphogenesis', *Acta Neuropathologica*. Acta Neuropathol, pp. 469–489. doi: 10.1007/s00401-013-1104-y.

Riska, B. (1986) 'Some models for development, growth, and morphometric correlation.', *Evolution*, 40(6), pp. 1303–1311. doi: 10.1111/j.1558-5646.1986.tb05753.x.

Roselló-Díez, A. and Joyner, A. L. (2015) 'Regulation of long bone growth in vertebrates; It is time to catch up', *Endocrine Reviews*. Endocrine Society, pp. 646–680. doi: 10.1210/er.2015-1048.

Ross, C. F. and Ravosa, M. J. (1993) 'Basicranial flexion, relative brain size, and facial kyphosis in nonhuman primates', *American Journal of Physical Anthropology*, 91(3), pp. 305–324. doi: 10.1002/ajpa.1330910306.

Schlager, S. (2017) 'Morpho and Rvcg - Shape Analysis in R: R-Packages for Geometric Morphometrics, Shape Analysis and Surface Manipulations', in *Statistical Shape and Deformation Analysis: Methods, Implementation and Applications*. Elsevier Inc., pp. 217–

bioRxiv preprint doi: https://doi.org/10.1101/2020.10.01.321604; this version posted October 1, 2020. The copyright holder for this preprint (which was not certified by peer review) is the author/funder, who has granted bioRxiv a license to display the preprint in perpetuity. It is made available under aCC-BY-NC-ND 4.0 International license.

256. doi: 10.1016/B978-0-12-810493-4.00011-0.

Schlager, S. (2020) 'Morpho: calculations and visualizations related to geometric morphometrics. R package version 2.8.' Available at: https://rdrr.io/cran/Morpho/.

Schmidt, M. J. *et al.* (2013) 'COMPARISON OF CLOSURE TIMES FOR CRANIAL BASE SYNCHONDROSES IN MESATICEPHALIC, BRACHYCEPHALIC, AND CAVALIER KING CHARLES SPANIEL DOGS', *Veterinary Radiology & Ultrasound*, 54(5), pp. 497–503. doi: 10.1111/vru.12072.

Scott, J. H. (1958) 'The cranial base', *American Journal of Physical Anthropology*, 16(3), pp. 319–348. doi: 10.1002/ajpa.1330160305.

Siegel, M. I. *et al.* (1985) 'Traction, prenatal development, and the labioseptopremaxillary region', *Plastic and Reconstructive Surgery*, 76(1), pp. 25–28. doi: 10.1097/00006534-198507000-00004.

Singh, N. *et al.* (2012) 'Morphological evolution through integration: A quantitative study of cranial integration in Homo, Pan, Gorilla and Pongo', *Journal of Human Evolution*, 62(1), pp. 155–164. doi: 10.1016/j.jhevol.2011.11.006.

Sparrow, L. M. *et al.* (2017) 'Gait changes in a line of mice artificially selected for longer limbs', *PeerJ*, 2017(2). doi: 10.7717/peerj.3008.

Vora, S. R. (2017) 'Mouse models for the study of cranial base growth and anomalies', *Orthodontics & Craniofacial Research*, 20, pp. 18–25. doi: 10.1111/ocr.12180.

Vora, S. R., Camci, E. D. and Cox, T. C. (2016) 'Postnatal Ontogeny of the Cranial Base and Craniofacial Skeleton in Male C57BL/6J Mice: A Reference Standard for Quantitative

bioRxiv preprint doi: https://doi.org/10.1101/2020.10.01.321604; this version posted October 1, 2020. The copyright holder for this preprint (which was not certified by peer review) is the author/funder, who has granted bioRxiv a license to display the preprint in perpetuity. It is made available under aCC-BY-NC-ND 4.0 International license.

Analysis', *Frontiers in Physiology*, 6(JAN), p. 417. doi: 10.3389/fphys.2015.00417.

Wagner, G. P. (1984) 'Coevolution of functionally constrained characters: Prerequisites for adaptive versatility', *BioSystems*, 17(1), pp. 51–55. doi: 10.1016/0303-2647(84)90015-7.

Wagner, G. P., Pavlicev, M. and Cheverud, J. M. (2007) 'The road to modularity', *Nature Reviews Genetics*. Nat Rev Genet, pp. 921–931. doi: 10.1038/nrg2267.

Waters, M. J. and Kaye, P. L. (2002) 'The role of growth hormone in fetal development', *Growth Hormone and IGF Research*. Churchill Livingstone, pp. 137–146. doi: 10.1016/S1096-6374(02)00018-7.

Wealthall, R. J. and Herring, S. W. (2006) 'Endochondral ossification of the mouse nasal septum', *The Anatomical Record Part A: Discoveries in Molecular, Cellular, and Evolutionary Biology*, 288A(11), pp. 1163–1172. doi: 10.1002/ar.a.20385.

Wei, X. *et al.* (2016) 'Developmental regulation of the growth plate and cranial synchondrosis', *Journal of Dental Research*, 95(11), pp. 1221–1229. doi: 10.1177/0022034516651823.

White, A. and Wallis, G. (2001) 'Endochondral ossification: A delicate balance between growth and mineralisation', *Current Biology*. Cell Press. doi: 10.1016/S0960-9822(01)00359-1.

Young, B. *et al.* (2006) 'Indian and sonic hedgehogs regulate synchondrosis growth plate and cranial base development and function', *Developmental Biology*, 299(1), pp. 272–282. doi: 10.1016/j.ydbio.2006.07.028.

Young, N. M. and Hallgrímsson, B. (2005) 'Serial Homology and The Evolution of Mammalian Limb Covariation Structure', *Evolution*, 59(12), pp. 2691–2704. doi: 10.1111/j.0014-3820.2005.tb00980.x.

bioRxiv preprint doi: https://doi.org/10.1101/2020.10.01.321604; this version posted October 1, 2020. The copyright holder for this preprint (which was not certified by peer review) is the author/funder, who has granted bioRxiv a license to display the preprint in perpetuity. It is made available under aCC-BY-NC-ND 4.0 International license.

**Table 1** – Longshanks adult (F01, F09, F20) and neonate (F32) sample composition.

| **Longshanks Samples (n)** | | | |
|---|---|---|---|
| | CTL | LS1 | LS2 |
| Generation 1 (F01) | 24 | 40 | 40 |
| Generation 9 (F09) | 23 | 40 | 40 |
| Generation 20 (F20) | 40 | 40 | 40 |
| Generation 32 (F32) | 32 | 36 | 36 |

bioRxiv preprint doi: https://doi.org/10.1101/2020.10.01.321604; this version posted October 1, 2020. The copyright holder for this preprint (which was not certified by peer review) is the author/funder, who has granted bioRxiv a license to display the preprint in perpetuity. It is made available under aCC-BY-NC-ND 4.0 International license.

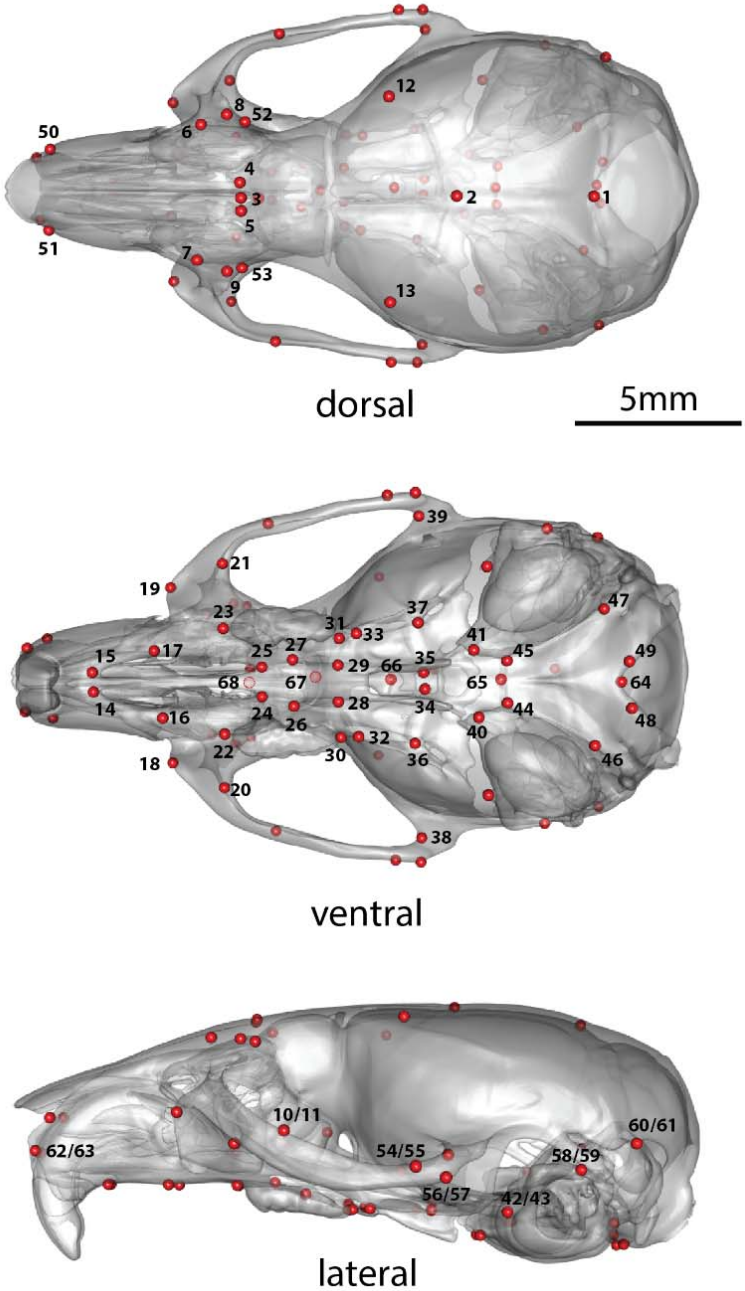


**Supplemental Figure 1** – Adult cranium landmarks used in this study in lateral, dorsal and ventral landmark views. For landmark anatomical definitions, see Supplementary Table 1.

bioRxiv preprint doi: https://doi.org/10.1101/2020.10.01.321604; this version posted October 1, 2020. The copyright holder for this preprint (which was not certified by peer review) is the author/funder, who has granted bioRxiv a license to display the preprint in perpetuity. It is made available under aCC-BY-NC-ND 4.0 International license.

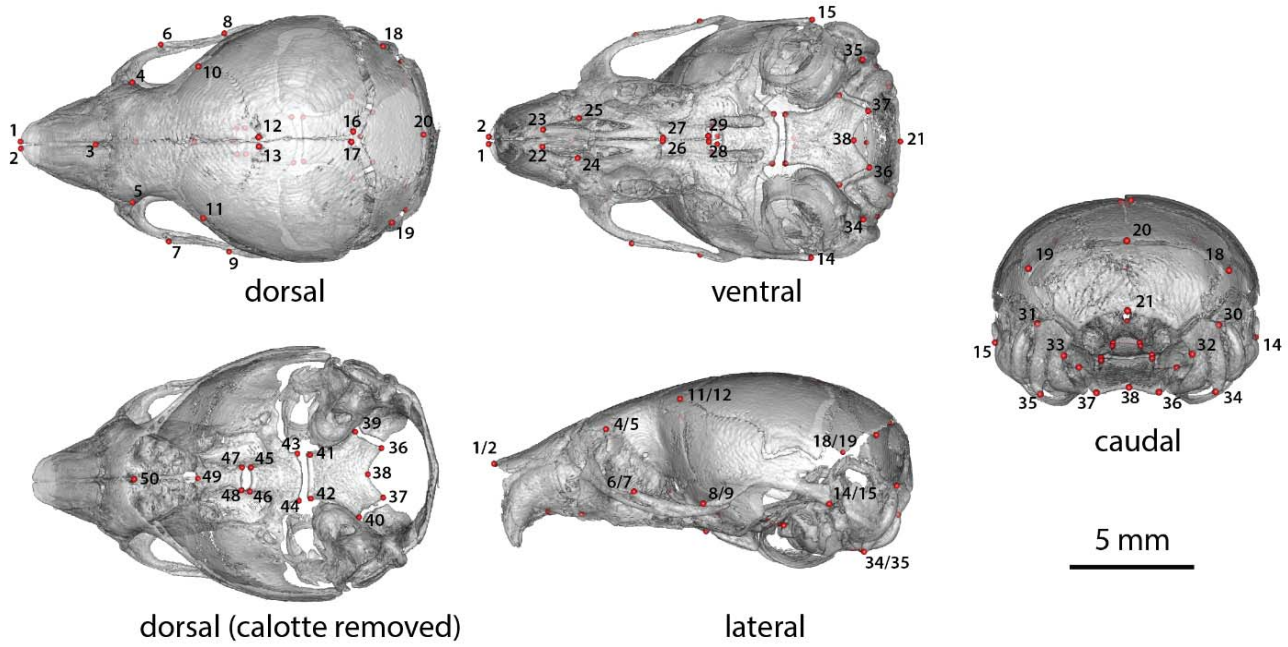


**Supplemental Figure 2** – Neonate (P07) cranium landmarks used in this study in lateral, dorsal, dorsal cranial base, caudal and ventral landmark views. For landmark anatomical definitions, see Supplementary Table 2.

bioRxiv preprint doi: https://doi.org/10.1101/2020.10.01.321604; this version posted October 1, 2020. The copyright holder for this preprint (which was not certified by peer review) is the author/funder, who has granted bioRxiv a license to display the preprint in perpetuity. It is made available under aCC-BY-NC-ND 4.0 International license.

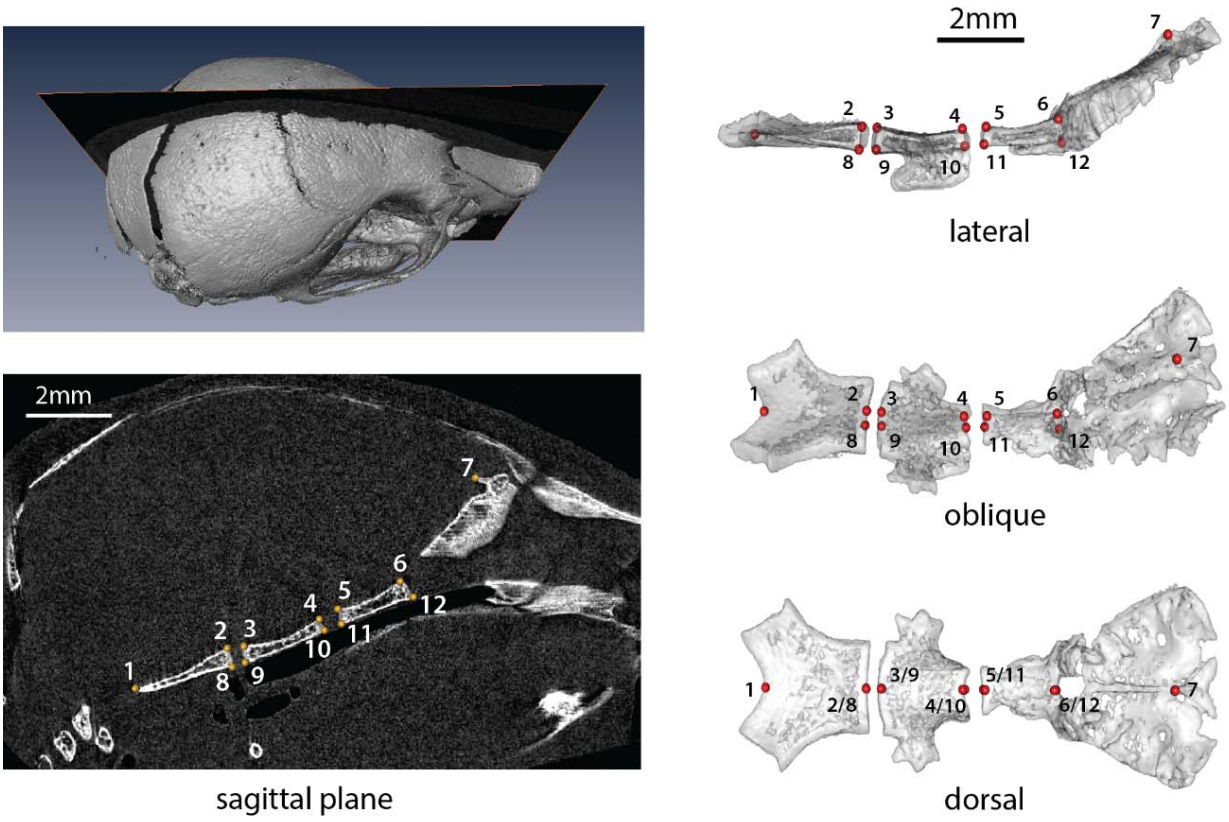


**Supplemental Figure 3** – Neonate (P07) cranial base landmarks on the sagittal midline used in this study. Numbered landmarks applied to CT scan reconstruction slices at the midline (left) and landmarks numbered on a 3D cranial base mesh (right). For landmark anatomical definitions, see Supplementary Table 3.

bioRxiv preprint doi: https://doi.org/10.1101/2020.10.01.321604; this version posted October 1, 2020. The copyright holder for this preprint (which was not certified by peer review) is the author/funder, who has granted bioRxiv a license to display the preprint in perpetuity. It is made available under aCC-BY-NC-ND 4.0 International license.

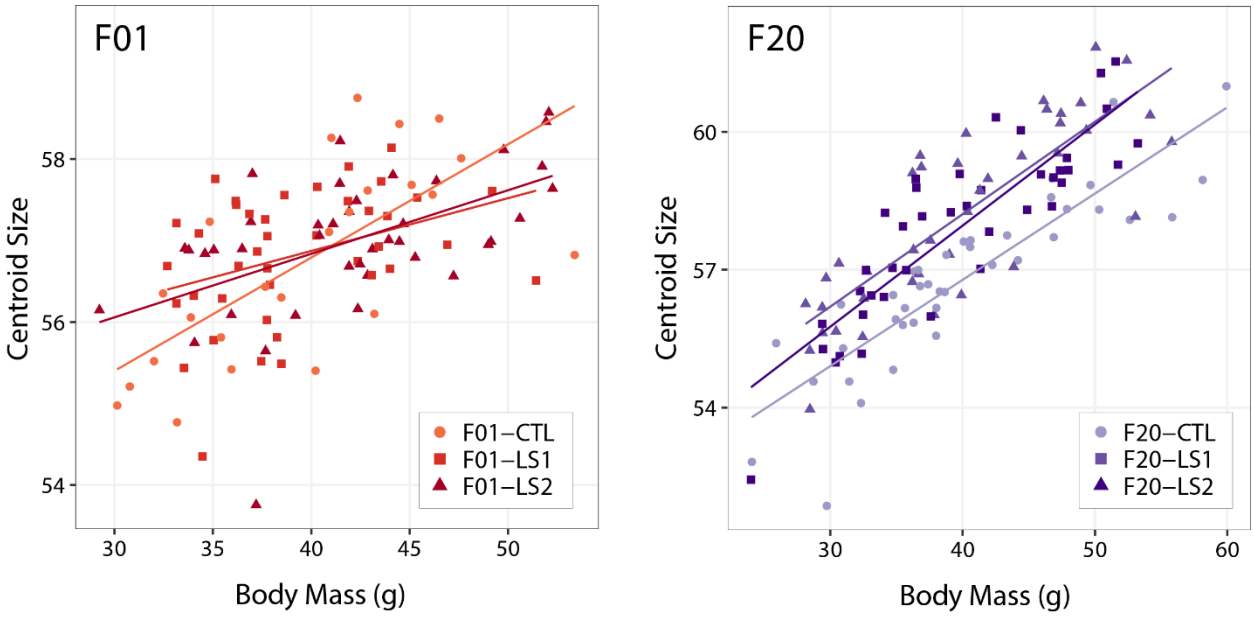


**Supplemental Figure 4** – Scatter plots with regression lines by group showing the relationships between body mass and cranium size (centroid size) in adult founder mice (F01) and after 20 generations of selection (F20).

bioRxiv preprint doi: https://doi.org/10.1101/2020.10.01.321604; this version posted October 1, 2020. The copyright holder for this preprint (which was not certified by peer review) is the author/funder, who has granted bioRxiv a license to display the preprint in perpetuity. It is made available under aCC-BY-NC-ND 4.0 International license.

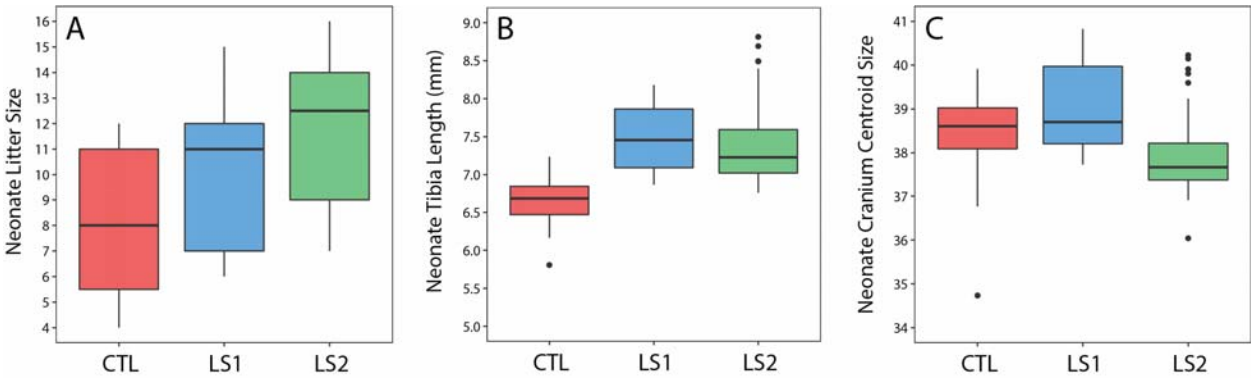


**Supplemental Figure 5** - Boxplots showing differences in neonate Longshanks and Control metrics. (A) Boxplot of neonate litter sizes. (B and C) Boxplots of litter size adjusted tibia length and cranium centroid size.

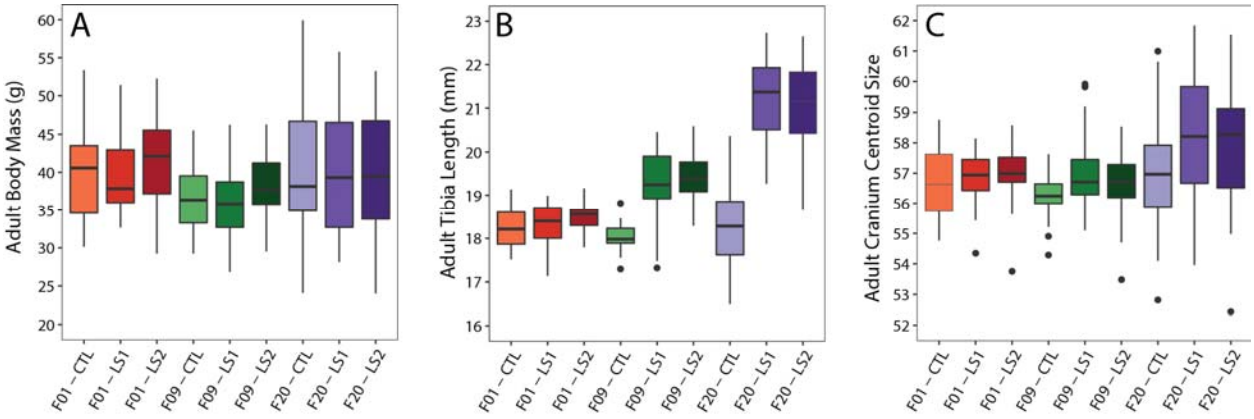


**Supplemental Figure 6** - Boxplots showing differences in adult Longshanks and Control metrics. (A-C) Boxplots of adult body mass, tibia length and cranial centroid size between groups.

bioRxiv preprint doi: https://doi.org/10.1101/2020.10.01.321604; this version posted October 1, 2020. The copyright holder for this preprint (which was not certified by peer review) is the author/funder, who has granted bioRxiv a license to display the preprint in perpetuity. It is made available under aCC-BY-NC-ND 4.0 International license.

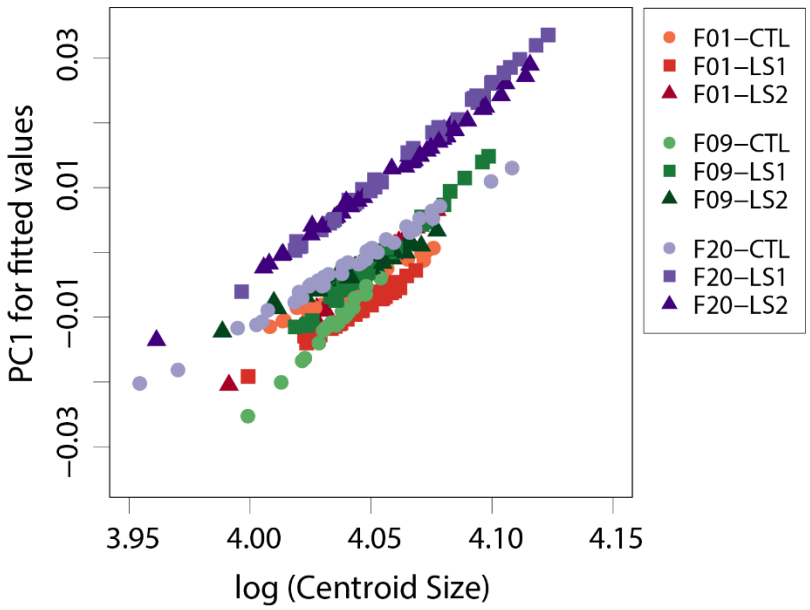


**Supplemental Figure 7** – Scatter plot of fitted PC1 scores (shape scores predicted by regression of shape on size) vs log (centroid size) showing within group patterns of cranium allometry. At any given cranium size, LS1 and LS2 are predicted to have positive shape scores (longer and narrower) shapes.

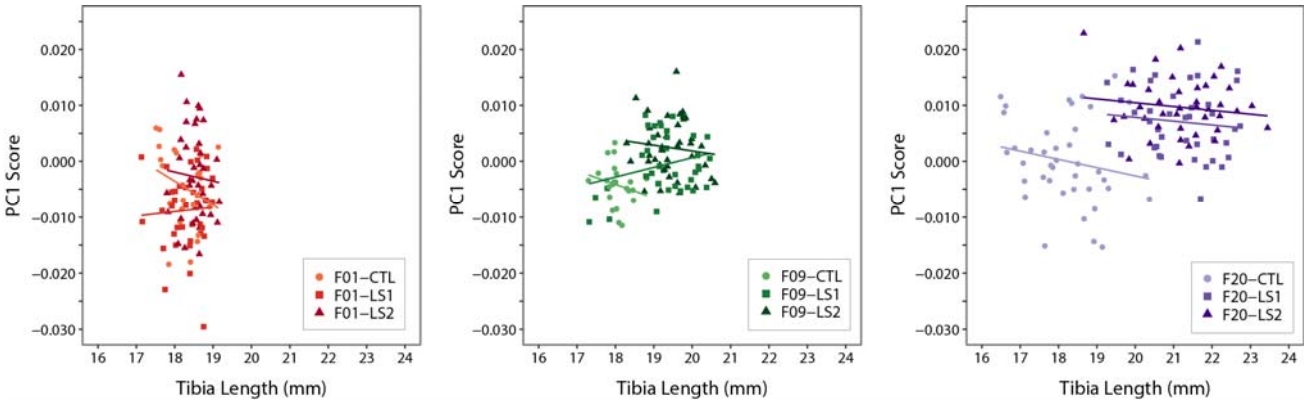


**Supplemental Figure 8** - Scatter plots with regression lines by group showing the relationships between PC1 score (cranium shape) and tibia length in adult mice throughout selection.

bioRxiv preprint doi: https://doi.org/10.1101/2020.10.01.321604; this version posted October 1, 2020. The copyright holder for this preprint (which was not certified by peer review) is the author/funder, who has granted bioRxiv a license to display the preprint in perpetuity. It is made available under aCC-BY-NC-ND 4.0 International license.

824 Table S1 – Adult cranium landmarks and their anatomical definitions.

| **Adult Cranium Landmarks** | |
|---|---|
| **Paired Landmarks (R/L)** | |
| Lateral point on frontal suture | 4/5 |
| Lateral zygomatic-frontal suture | 6/7 |
| Posterior zygomaticofrontal junction | 8/9 |
| Posterior margin of malar process | 10/11 |
| Frontal-temporal-parietal junction | 12/13 |
| Anterior margin of incisive foramen | 14/15 |
| Medial maxilla-premaxilla junction | 16/17 |
| Anterior inferior zygomatic | 18/19 |
| Anterior temporo-zygomatic junction | 20/21 |
| Anterior superior alveoli | 22/23 |
| Posterior incisive foramen | 24/25 |
| Point along palatine-maxillary suture | 26/27 |
| Medial palatal-pterygoid junction | 28/29 |
| Posterior superior alveoli | 30/31 |
| Lateral palatal-pterygoid junction | 32/33 |
| Spheno-occipital synchondrosis | 34/35 |
| Anterior foramen ovale | 36/37 |
| Posterior temporo-zygomatic junction | 38/39 |
| Auditory-temporal-sphenoid junction | 40/41 |
| Anterior inferior auditory bulla | 42/43 |
| Occipital-auditory-sphenoid junction | 44/45 |
| Point along occipitomastoid suture | 46/47 |
| Medial occipital condyle | 48/49 |
| Anterior nasal and premaxilla | 50/51 |
| Frontal suture on orbital rim | 52/53 |
| Superior temporo-zygomatic suture | 54/55 |
| Posterior zygomatic process | 56/57 |
| Superio-posterior tympanic ring | 58/59 |

bioRxiv preprint doi: https://doi.org/10.1101/2020.10.01.321604; this version posted October 1, 2020. The copyright holder for this preprint (which was not certified by peer review) is the author/funder, who has granted bioRxiv a license to display the preprint in perpetuity. It is made available under aCC-BY-NC-ND 4.0 International license.

| | |
|---|---|
| Occipital-auditory junction | 60/61 |
| Midline superior incisor | 62/63 |
| **Midline Landmarks** | |
| Lambda | 1 |
| Bregma | 2 |
| Nasion | 3 |
| Anterior foramen magnum | 64 |
| Midline junction basioccipital and sphenoid | 65 |
| Midline junction sphenoid and presphenoid | 66 |
| Anterior junction endocranial presphenoid | 67 |
| Endocranial junction frontal and ethmoid | 68 |

825

826 Table S2 – Neonate cranium landmarks and their anatomical definitions.

| **Neonate Cranium Landmarks** | |
|---|---|
| **Paired Landmarks (L/R)** | |
| Medial rostral tip of nasal bones | 1/2 |
| Caudal dorsal fronto-zygomatic suture on frontal bone | 4/5 |
| Rostral dorsal zygomatic suture on zygomatic bone | 6/7 |
| Caudal dorsal zygomatic suture on zygomatic process of temporal bone | 8/9 |
| Temporal-parietal-frontal suture | 10/11 |
| Caudal medial tip of frontal bones (bregma) | 12/13 |
| Ventral caudal tip of occipital process of temporal bone | 14/15 |
| Caudal medial tip of the parietal | 16/17 |
| Caudal lateral tip of interparietal | 18/19 |
| Rostral incisor foramen | 22/23 |
| Premaxilla-maxilla suture (rostral medial maxilla) | 24/25 |
| Maxilla-palatine suture (rostral medial palatine) | 26/27 |
| Caudal medial tip of palatine | 28/29 |
| Dorsal lateral tip of exoccipital | 30/31 |
| Medial border of exoccipital at widest mediolateral span of foramen magnum | 32/33 |
| Ventral tip of paraoccipital process | 34/35 |
| Caudal medial tip of basioccipital at intra-occipital synchondrosis | 36/37 |

bioRxiv preprint doi: https://doi.org/10.1101/2020.10.01.321604; this version posted October 1, 2020. The copyright holder for this preprint (which was not certified by peer review) is the author/funder, who has granted bioRxiv a license to display the preprint in perpetuity. It is made available under aCC-BY-NC-ND 4.0 International license.

| | |
|---|---|
| Caudal lateral tip of basioccipital at intra-occipital synchondrosis | 39/40 |
| Rostral lateral tip of basioccipital at spheno-occipital synchondrosis | 41/42 |
| Caudal lateral tip of sphenoid at spheno-occipital synchondrosis | 43/44 |
| Rostral lateral tip of sphenoid at inter-sphenoidal synchondrosis | 45/46 |
| Caudal lateral tip of presphenoid at inter-sphenoidal synchondrosis | 47/48 |
| **Midline Landmarks** | |
| Caudal medial nasal bones (nasion) | 3 |
| Caudal medial border of interparietal | 20 |
| Ventral medial occipital (dorsal foramen magnum) | 21 |
| Caudal medial border of basioccipital (rostral foramen magnum) | 38 |
| Ethmoid-presphenoid suture | 49 |
| Rostral medial border of cribriform plate | 50 |

bioRxiv preprint doi: https://doi.org/10.1101/2020.10.01.321604; this version posted October 1, 2020. The copyright holder for this preprint (which was not certified by peer review) is the author/funder, who has granted bioRxiv a license to display the preprint in perpetuity. It is made available under aCC-BY-NC-ND 4.0 International license.

Table S3 – Neonate cranial base landmarks and their anatomical definitions.

| **Sagittal Midline Neonate Cranial Base Landmarks** | |
|---|---|
| Basion | 1 |
| Rostral dorsal tip of basi-occipital at spheno-occipital synchondrosis | 2 |
| Caudal dorsal tip of basi-sphenoid at spheno-occipital synchondrosis | 3 |
| Rostral dorsal tip of basi-sphenoid at intersphenoidal synchondrosis | 4 |
| Caudal dorsal tip of presphenoid at intersphenoidal synchondrosis | 5 |
| Ethmoid-presphenoid suture | 6 |
| Rostral medial border of cribriform plate | 7 |
| Rostral ventral tip of basi-occipital at spheno-occipital synchondrosis | 8 |
| Caudal ventral tip of basi-sphenoid at spheno-occipital synchondrosis | 9 |
| Rostral ventral tip of basi-sphenoid at intersphenoidal synchondrosis | 10 |
| Caudal ventral tip of presphenoid at intersphenoidal synchondrosis | 11 |
| Rostral ventral tip of the presphenoid | 12 |

Table S4 – Morphometric data for neonate mice among lines and generations. Data represents least squared means (SEM). Superscripts denote significant differences in means ($p < 0.05$) between a given group and: Controls $^{CTL}$, Longshanks Line 1 $^{LS1}$, Longshanks Line 2 $^{LS2}$.

| **Neonate Morphometric Data** | | | |
|---|---|---|---|
| Line | CTL | LS1 | LS2 |
| Ossified Tibial Diaphysis Length (mm) | 6.66 (0.06) $^{LS1, LS2}$ | 7.50 (0.07) $^{CTL}$ | 7.41 (0.10) $^{CTL}$ |
| Litter Size | 7.94 (0.55) $^{LS1, LS2}$ | 10.33 (0.51) $^{CTL}$ | 11.83 (0.51) $^{CTL}$ |
| Centroid Size | 38.49 (0.17) $^{LS1}$ | 39.05 (0.16) $^{CTL, LS2}$ | 37.94 (0.16) $^{LS1}$ |

bioRxiv preprint doi: https://doi.org/10.1101/2020.10.01.321604; this version posted October 1, 2020. The copyright holder for this preprint (which was not certified by peer review) is the author/funder, who has granted bioRxiv a license to display the preprint in perpetuity. It is made available under aCC-BY-NC-ND 4.0 International license.

Table S5 – Morphometric data for adult mice among lines and generations. Body mass data represent means and SEM, whereas centroid size and tibia length are least squared means and SEM. Superscripts denote significant differences in means ($p < 0.05$) between a given group and: Controls $^{CTL}$, Longshanks Line 1 $^{LS1}$, Longshanks Line 2 $^{LS2}$, from either: Generation 1 $^{F01}$, Generation 9 $^{F09}$, or Generation 20 $^{F20}$. Bold and italic superscripts indicate significant intergenerational differences and intragenerational differences, respectively.

| **Adult Body Mass (g)** | | | |
|---|---|---|---|
| Generation | CTL | LS1 | LS2 |
| F01 | 39.61 (1.28) | 39.25 (0.99) | 42.13 (0.99) **F09 CTL, F09 LS2** |
| F09 | 36.54 (1.30) **F01 LS2** | 35.91 (0.99) | 38.33 (0.99) **F01 LS2** |
| F20 | 40.05 (0.99) | 39.89 (0.99) | 39.81 (0.99) |

| **Adult Tibia Length (mm)** | | | |
|---|---|---|---|
| Generation | CTL | LS1 | LS2 |
| F01 | 18.21 (0.12) | 18.32 (0.09) **F09-LS1, F20-LS1** | 18.30 (0.09) **F09-LS2, F20-LS2** |
| F09 | 18.23 (0.12) *F09-LS1, F09-LS2* | 19.51 (0.09) **F01-LS1, F20-LS1**, *F09-CTL* | 19.50 (0.09) **F01-LS2, F20-LS2**, *F09-CTL* |
| F20 | 18.13 (0.09) *F20-LS1, F20-LS2* | 21.13 (0.09) **F01-LS1, F09-LS1**, *F20-CTL* | 21.15 (0.09) **F01-LS2, F09-LS2**, *F20-CTL* |

| **Adult Cranial Centroid Size** | | | |
|---|---|---|---|
| Generation | CTL | LS1 | LS2 |
| F01 | 56.66 (0.19) | 56.81 (0.15) **F20-LS1** | 56.51 (0.15) **F20-LS2** |
| F09 | 56.64 (0.19) | 57.49 (0.15) **F20-LS1** | 56.82 (0.15) **F20-LS2** |
| F20 | 56.64 (0.15) *F20-LS1, F20-LS2* | 58.07 (0.15) **F01-LS1, F09-LS1**, *F20-CTL* | 57.81 (0.15) **F01-LS2, F09-LS2**, *F20-CTL* |

bioRxiv preprint doi: https://doi.org/10.1101/2020.10.01.321604; this version posted October 1, 2020. The copyright holder for this preprint (which was not certified by peer review) is the author/funder, who has granted bioRxiv a license to display the preprint in perpetuity. It is made available under aCC-BY-NC-ND 4.0 International license.

Supplementary Table S6: Euclidean distance between the multivariate mean PC scores of each group, based on Procrustes shape data adjusted for sex only (above diagonal), or sex and cranial centroid size (below diagonal). The only non-significant Euclidean distance, based on a post-hoc Procrustes ANCOVA, is indicated in bold.

| | **Mean PC scores adjusted for sex only** | | | | | | | | | |
|---|---|---|---|---|---|---|---|---|---|---|
| **Mean PC scores adjusted for centroid size and sex** | | F01-CTL | F01-LS1 | F01-LS2 | F09-CTL | F09-LS1 | F09-LS2 | F20-CTL | F20-LS1 | F20-LS2 |
| | F01-CTL | - | 0.010 | **0.007** | 0.012 | 0.013 | 0.015 | 0.010 | 0.022 | 0.023 |
| | F01-LS1 | 0.011 | - | 0.011 | 0.014 | 0.016 | 0.018 | 0.014 | 0.025 | 0.026 |
| | F01-LS2 | **0.007** | 0.011 | - | 0.012 | 0.011 | 0.013 | 0.009 | 0.020 | 0.020 |
| | F09-CTL | 0.011 | 0.014 | 0.010 | - | 0.012 | 0.012 | 0.013 | 0.027 | 0.026 |
| | F09-LS1 | 0.013 | 0.016 | 0.011 | 0.010 | - | 0.011 | 0.014 | 0.020 | 0.021 |
| | F09-LS2 | 0.015 | 0.018 | 0.013 | 0.011 | 0.011 | - | 0.013 | 0.023 | 0.018 |
| | F20-CTL | 0.010 | 0.014 | 0.010 | 0.012 | 0.014 | 0.013 | - | 0.021 | 0.019 |
| | F20-LS1 | 0.016 | 0.020 | 0.015 | 0.018 | 0.015 | 0.018 | 0.015 | - | 0.015 |
| | F20-LS2 | 0.018 | 0.022 | 0.016 | 0.019 | 0.018 | 0.013 | 0.014 | 0.015 | - |